MENU

NPG asia materials

Search | E-alert | Submit | Login

Featured article: Polymers: Printable self-healing devices

A soft material that can heal itself when damaged has been 3D printed by researchers in the USA.

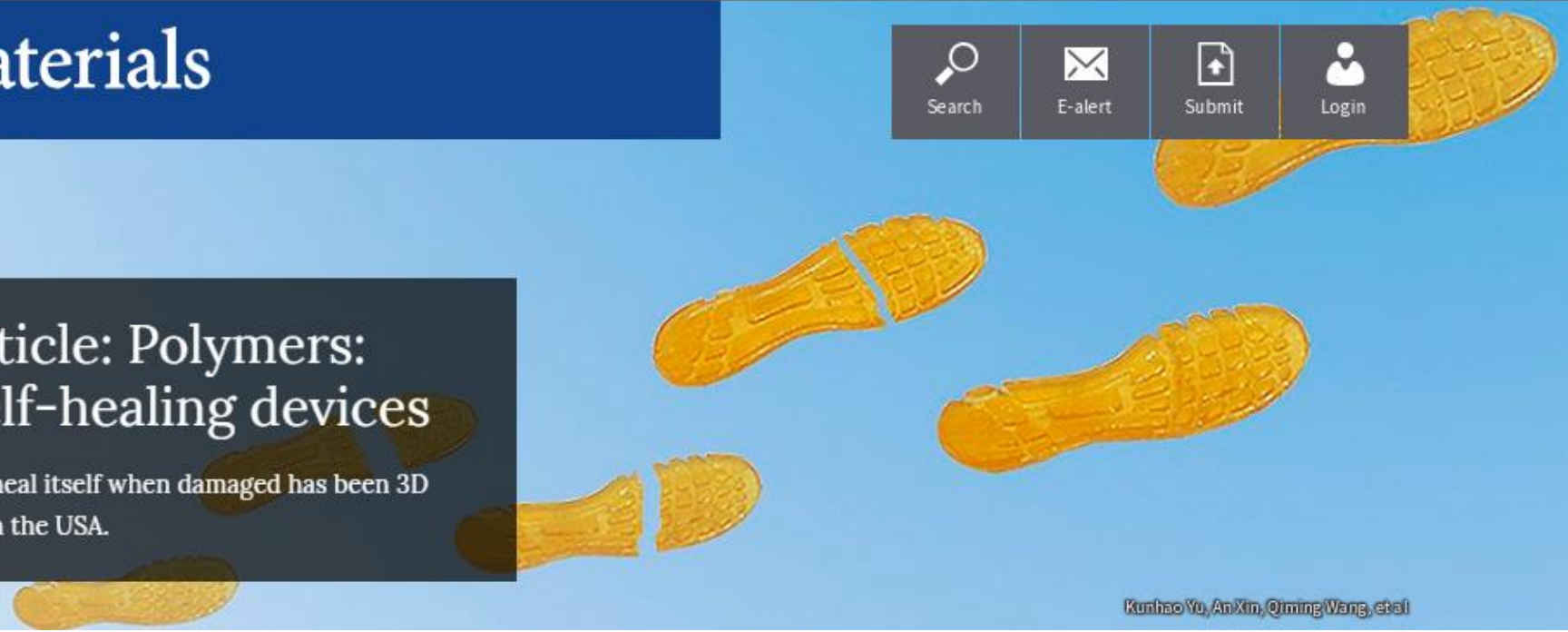

Kunhao Yu, An Xin, Qiming Wang, et al

Yu et al. *NPG Asia Materials* (2019)11:7
https://doi.org/10.1038/s41427-019-0109-y

NPG Asia Materials

ARTICLE Open Access

Additive manufacturing of self-healing elastomers

Kunhao Yu[1], An Xin[1], Haixu Du[1], Ying Li[2] and Qiming Wang[1]

Abstract

Nature excels in both self-healing and 3D shaping; for example, self-healable human organs feature functional geometries and microstructures. However, tailoring man-made self-healing materials into complex structures faces substantial challenges. Here, we report a paradigm of photopolymerization-based additive manufacturing of self-healable elastomer structures with free-form architectures. The paradigm relies on a molecularly designed photoelastomer ink with both thiol and disulfide groups, where the former facilitates a thiol-ene photopolymerization during the additive manufacturing process and the latter enables a disulfide metathesis reaction during the self-healing process. We find that the competition between the thiol and disulfide groups governs the photocuring rate and self-healing efficiency of the photoelastomer. The self-healing behavior of the photoelastomer is understood with a theoretical model that agrees well with the experimental results. With projection microstereolithography systems, we demonstrate rapid additive manufacturing of single- and multimaterial self-healable structures for 3D soft actuators, multiphase composites, and architected electronics. Compatible with various photopolymerization-based additive manufacturing systems, the photoelastomer is expected to open promising avenues for fabricating structures where free-form architectures and efficient self-healing are both desirable.

Introduction

Natural living materials, such as animal organs, can autonomously self-heal wounds. Inspired by natural living materials, scientists have developed synthetic self-healing polymers capable of repairing fractures or damages at the microscopic scale and restoring mechanical strengths at the macroscopic scale[1–3]. The healing capability usually relies on extrinsic curing-agent encapsulates released upon fractures[4,5] or on intrinsic dynamic bonds, such as dynamic covalent bonds[6,7] and physical bonds[8–15], that autonomously reform after fracture-induced dissociations. Thanks to their healing capability, these polymers have enabled a wide range of applications, such as flexible electronics[16–18], energy transducers[12,19], soft robotics[20,21], lithium batteries[22], water membranes[23], and biomedical devices[24]. Despite the success in syntheses and applications, the existing self-healing polymers are still facing a critical bottleneck—deficiency in 3D shaping. This bottleneck makes synthetic self-healing polymers different from living materials (such as human organs) that usually feature functional geometries and microstructures. Additionally, a number of promising applications of self-healing polymers demand complex 2D/3D architectures, such as soft robotics[20,25], structural composites[26,27], and architected electronics[28]. However, the architecture demand of self-healing polymers has not been sufficiently fulfilled, as the existing 3D methods of shaping self-healing polymers include only molding[17] and direct-writing[29–32], which are either time consuming or limited in their formation of complex 3D architectures[33,34].

Here, we report a strategy for photopolymerization-based additive manufacturing (AM) of self-healing elastomer structures with free-form architectures. The strategy relies on a molecularly designed photoelastomer ink with both thiol and disulfide groups, where the former

Correspondence: Qiming Wang (qimingw@usc.edu)
[1]Sonny Astani Department of Civil and Environmental Engineering, University of Southern California, Los Angeles, CA 90089, USA
[2]Department of Mechanical Engineering and Institute of Materials Science, University of Connecticut, Storrs, CT 06269, USA

facilitates a thiol-ene photopolymerization during the AM process and the latter enables a disulfide metathesis reaction during the self-healing process. Using projection microstereolithography systems, we demonstrate the rapid AM of single- and multimaterial elastomer structures in various 3D complex geometries within a short time (e.g., 0.6 mm × 15 mm × 15 mm/min = 13.5 mm^3/min). These structures can rapidly heal the fractures and restore their initial structural integrity and mechanical strengths to 100%. We find that the competition between the thiol and disulfide groups governs the photocuring rate and self-healing efficiency of the photoelastomer. The self-healing behavior of the photoelastomer is understood with a theoretical model that agrees well with the experimental results. To demonstrate potential applications of the 3D-printable self-healing elastomers, we present a self-healable 3D soft actuator that can lift a weight ten times its own weight, a nacre-like stiff-soft composite that restores the toughness to over 90% after fracture, and a self-healable force sensor with both dielectric and conductive phases. Equipped with the capability of rapid photopolymerization that is compatible with various AM systems, such as stereolithography[35,36], self-propagation photopolymer waveguide[37,38], two-photon lithography[39,40], and PolyJet printing[41], the new self-healing photoelastomer system is expected to open promising avenues for fabricating structures where free-form architecture and efficient self-healing are both desirable[20,42].

Materials and methods

Materials

Vinyl-terminated polydimethylsiloxanes (V-PDMS, molar mass 6000–20,000 g/mol) and [4–6% (mercaptopropyl)methylsiloxane]-dimethylsiloxane (MMDS) were purchased from Gelest. Iodobenzene diacetate (IBDA), toluene, tributylphosphine (TBP), 1,6-hexanediol diacrylate (HDDA), phenylbis(2,4,6-trimethylbenzoyl)phosphine oxide (photoinitiator), Sudan I (photoabsorber), and ethanol were purchased from Sigma-Aldrich. The chemicals were used as purchased without further purification. Carbon grease was purchased from GM chemicals.

Synthesis and characterization of material inks

To prepare the experimental elastomer ink, 0.5 g of IBDA was first mixed with 5 mL of toluene in a nitrogen environment with magnetic stirring for 6 h. Then, 1 g of MMDS was oxidized by adding different amounts of the IBDA solution (0 g, 0.35 g, 0.7 g, 1 g, and 1.2 g) for 1 min. Subsequently, 1.95 g of V-PDMS, 1 wt% photoinitiator, and 0.1 wt% photoabsorber were added and mixed for another 1 min. The 0.1 wt% of TBP was then added and mixed for another 1 min. To prepare the control elastomer ink, 1 g of MMDS, 1.95 g of V-PDMS, 1 wt% photoinitiator, and 0.1 wt% photoabsorber were mixed for 5 min. Raman spectroscopy measurements were performed using a Horiba Raman infrared microscope with an acquisition time of 1 min. The spectra of the material inks from 200 to 1800 cm^{-1} were collected using a laser excitation wavelength of 532 nm.

Additive manufacturing

The single- and multimaterial stereolithography systems were described elsewhere[35,36]. To fabricate the multimaterial structures, we first divided the computer-aided-design (CAD) model of a biphase composite into two models with respective phases. Each phase model was then sliced into an image sequence with a prescribed spacing in the vertical direction. Then, two image sequences were alternatively integrated into one image sequence. The images were sequentially projected onto a resin bath that was filled with a material ink. The ink capped with a motor-controlled printing stage was exposed to the image light (405 nm) and solidified to form a layer structure bonded to the printing stage. As the printing stage was lifted up, the wheel was rotated to deliver the ethanol beneath the printing stage. With the printing stage lowered into the ethanol, the printed structure was washed, and the ethanol residue was subsequently absorbed by the cotton pad. Then, another material ink was delivered beneath the stage by the rotational wheel. By lowering the stage by a prescribed height and illuminating another image, a second material layer could be printed on the existing structures. By repeating these processes, we printed multimaterial structures. To fabricate single-material structures, we just simplified the process by using one image sequence and removing the intermediate cleaning process. Note that a traditional stereolithography system with acrylic-based resins has an oxygen-rich layer to quench the photopolymerization close to the printing window[43], and this oxygen-rich layer can facilitate the manufacturing process by reducing the adhesion between the printed part and the window[43]. However, the thiol-ene photopolymerization system cannot be quenched by the oxygen[44]. To enable easy separation between the solidified part and the window, we employ a Teflon membrane with a low surface tension (~20 mN/m) to enable low separation forces. In addition, all fabricated samples were heated for 2 h at 60 °C to remove the residual toluene and ethanol and then postcured in a UV chamber for an additional 1 h (same wavelength as the AM system) to ensure the samples were fully polymerized.

Photocuring depth test

A 10 mm × 10 mm square image was illuminated on the printing window using different photoexposure times for the experimental elastomers with various IBDA

concentrations. The thicknesses of the photocured parts were measured at the cross-sections by using an optical microscope (Nikon ECLIPSE LV100ND).

Self-healing test

The dog-bone-shaped samples (thickness 4 mm) were first additively manufactured. Then, the samples were cut into two pieces with a blade and brought into contact with an additional force (~0.5 N) on two sides to ensure good contact. The samples were then put on a hot plate at 60 °C for various healing times. Both the original and healed samples were clamped by using two rigid plates in a tensile testing machine (Instron 5942) to be uniaxially stretched until rupture with a low strain rate of 0.06 s^{-1}. The microscopic images of the damaged and healed interfaces were taken with an optical microscope (Nikon Eclipse LV100ND).

Mechanical test of the experimental elastomer

The storage and loss moduli of the experimental elastomer at frequencies of 0.1–10 Hz and temperatures of 25–165 °C were tested using a dynamic mechanical analyzer (TA instrument RSA III). The cyclic tensile tests of the experimental elastomer were conducted using an Instron 5942 with a low strain rate of 0.006 s^{-1}.

Self-healable actuator

The 3D actuator was first designed and additively manufactured. A 10 g weight was hanged at the bottom of the actuator that was connected to a syringe pump. When the syringe pump was moved, the weight was lifted up. A camera was used to image the distance change of the weight. Then, we cut the actuator in half with a blade and contacted back to heal for 2 h at 60 °C. Once healed, the actuator was used to lift the 10 g weight again for multiple cycles.

Self-healable composite

The experimental composites (width 10 mm, length 15 mm, and thickness 1 mm) with stiff phase HDDA and soft phase self-healing elastomer were first additively manufactured. Then, a small notch was made at the center edge of the samples. The notched samples were clamped and stretched in the Instron tensile tester with a low strain rate of 0.06 s^{-1}. The first group of control samples included pure HDDAs and self-healing elastomers that were the same size as the experimental composites. The second group of the control samples included composite samples with stiff phase HDDA and soft phase non-self-healing elastomer (also the same size as the experimental composites). These two control sample groups underwent similar tensile tests as the experimental composites.

Self-healable electronics

The self-healable conductive elastomer ink was synthesized by adding 50 wt% carbon grease to the self-healing elastomer ink. The self-healable conductive elastomer samples were fabricated using the single-material stereolithography system. A University of Southern California (USC) Trojan pad was fabricated (width 10 mm, length 10 mm, and thickness 1 mm) with the dielectric phase self-healing elastomer and the conductive phase conductive elastomer was fabricated using the multi-material stereolithography system. The resistance was measured with a source meter (Keithley 2400). The voltage (10 V AC) for powering the LED was provided by the source meter. The force sensor was fabricated by laminating the Trojan pad between of two same-size, self-healable elastomer pads. A compressive force was applied and measured by the Instron machine with two plastic compression plates.

Results

Molecular design of the self-healable photoelastomer

The molecular design of the self-healing elastomer with integrated photopolymerization and self-healing features is based on the coexistence of thiol (R-S-H) and disulfide (R-S-S-R′) groups (Fig. 1a). The photopolymerization is achieved by harnessing the high-rate and high-yield thiol-ene crosslinking reaction in which the thiol groups (R-S-H) and alkene groups (H_2-C = C-HR′) react to form alkyl sulfides (R-S-C-C-H_2R′) under the photoinduced radical initiation (Fig. 1a, b)[44]. Efficient self-healing is achieved by harnessing dynamic disulfide bonds that undergo disulfide metathesis reactions (assisted by a catalyst tributylphosphine) to bridge the fractured interface (Fig. 1c)[45]. To introduce the disulfide groups in the polymer network, we partially oxidize the thiol groups using a highly efficient oxidant, iodobenzene diacetate (IBDA) (Fig. 1a)[46,47]. After the partial oxidation, the thiol and disulfide groups coexist in the material ink to form thiol-disulfide oligomers. After the photopolymerization, the dynamic disulfide bonds will be covalently integrated within the crosslinker regions (Fig. 1a).

To prove the concept, we employed [4–6% (mercaptopropyl)methylsiloxane]-dimethylsiloxane copolymer (MMDS, Fig. S1a) and vinyl-terminated polydimethylsiloxane (V-PDMS, Fig. S1b) to provide the thiol groups and alkene groups, respectively[48,49]. Both chemicals have relatively low viscosities (below 200 cSt) that are suitable for the stereolithography process. V-PDMS, which has a relatively high molar mass (6000–20,000 g/mol), constitutes the polymer backbone and enables the high flexibility and stretchability of the elastomer. The material ink is used in a projection microstereolithography system to enable the rapid

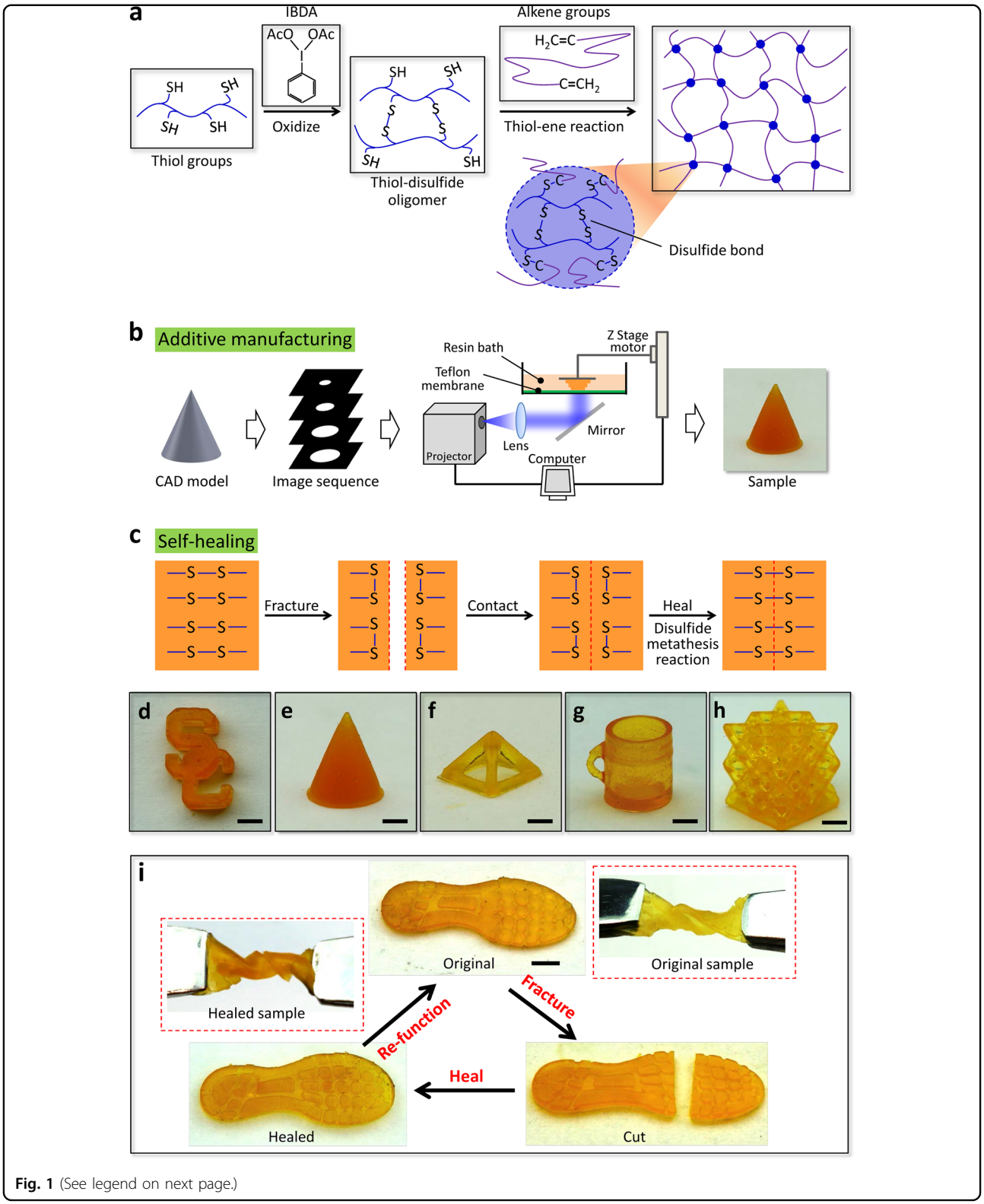

Fig. 1 (See legend on next page.)

(see figure on previous page)
Fig. 1 Additive manufacturing of self-healing elastomers. a Molecular design of the self-healing elastomer. MMDS with thiol groups was first oxidized with the IBDA to form a thiol-disulfide oligomer. The oligomer then undergoes a photoinitiated thiol-ene reaction with the V-PDMS with alkene groups to form a solid elastomer. The elastomer embeds dynamic disulfide bonds within the crosslinker region. **b** Stereolithography-based additive manufacturing process. An image sequence sliced from a computer-aided-design (CAD) model is sequentially projected onto a resin bath to form a layer-by-layer structure. **c** Schematics to show the disulfide bond enabled self-healing process. The fractured interface can be healed through a disulfide metathesis reaction. **d**–**h** The manufactured samples: **d** a logo of the University of Southern California, **e** a circular cone, **f** a pyramid lattice unit, **g** a cup, and **h** an octet truss lattice. **i** Self-healing of a shoe pad sample. The fabricated shoe pad can sustain a 540-degree twist. Once cut, the shoe pad is brought into contact to heal for 2 h at 60 °C. Then, the healed shoe pad can sustain the 540-degree twist again. The scale bars in (**d**–**i**) represent 4 mm

prototyping of various 2D/3D elastomer structures, including a logo of the University of Southern California (Fig. 1d), a circular cone (Fig. 1e), a pyramid (Fig. 1f), a cup (Fig. 1g), and an octet truss lattice (Fig. 1h). The manufacturing process is rapid with a speed of ~25 μm/s for each layer and approximately 5–60 min for each structure shown in Fig. 1d–h. The manufacturing resolution can reach as low as 13.5 μm (Fig. S2). The elastomer not only can be 3D printed to nearly any 3D architecture but can also self-heal fatal fractures. As a simple demonstration in Fig. 1i, we fabricate a delicately patterned shoe pad that can be flexibly twisted by 540 degrees. We then cut the pad into two parts and contact back to heal for 2 h at 60 °C. After the healing process, the sample can sustain the 540-degree twist again.

Characterization of the self-healing property

Next, we characterize the self-healing property of the synthesized photoelastomer (Fig. 2). We design two types of photoelastomers: experimental elastomers with IBDA-enabled disulfide bonds (Fig. 1a) and control elastomers without the disulfide bonds (the molecular structure in Fig. S3). Both elastomer inks can be 3D printed into dog-bone-shaped samples (Fig. 2a). Then, we cut the samples into two parts and brought them into contact for various healing times (0–270 min) at 60 °C. Subsequently, the samples were uniaxially stretched until rupture. We can verify the self-healing property of the experimental elastomer from three aspects. First, the existence of the disulfide bond in the experimental elastomer was verified by Raman spectroscopy measurements that show a new peak with a band at ~520 cm^{-1} (Fig. S4). This new band is consistent with the Raman band in the reported disulfide-bond-enabled self-healing polymers (500–550 cm^{-1})[50,51]. Second, microscopic images show that the crack gap of the fractured experimental elastomer is nicely bridged after 2 h of healing at 60 °C (Fig. 2b, c). Third, we find that the tensile strengths of the experimental elastomers gradually increase with increasing healing time until a plateau at ~100% of the original strength after 60 min (Fig. 2d). However, the tensile strengths of the control elastomers reach a plateau of only 40% of the original strength after 60 min at 60 °C (Fig. 2e, f). This result shows that the dynamic disulfide bonds play a central role in healing the fractured interface to restore 100% strength. Without the disulfide-bond-enabled interfacial bridging, the interfacial bonding of the control elastomer possibly stems from the noncrosslinking chain entanglement around the fracture interface[52]; however, this chain entanglement effect cannot lead to 100% interfacial self-healing.

For the experimental elastomer, we can further carry out self-healing tests for more than 10 cycles, and the corresponding healing strength ratios (tensile strength of the healed sample over that of the original sample) remain at 90–100% (Fig. 2g and S5a). It is also noted that due to the solvent-free character, the elastomer samples do not show any visible volume shrinkage during the 10-cycle healing process (each 2 h at 60 °C) (Fig. S5b). This character enables the self-healing elastomer to be intrinsically different from the reported directly written self-healing hydrogels[29–31]. In addition, we find that the mechanical properties of the experimental elastomer remain almost unchanged after being immersed in DI water for 24 h (Fig. S6), which makes these elastomers dramatically different from the moisture-sensitive self-healing elastomers with hydrogen bonds[9,16].

Although the experimental elastomer displays a relatively low Young's modulus (~17.4 kPa), the frequency sweep test verifies that its storage modulus (Young's modulus) is much larger than the loss modulus (500–600 Pa) over a wide frequency range (0.1–10 Hz) (Fig. S7a). This result shows that the elastic character of the experimental elastomer dominates the viscous character. Additionally, we further test the storage-loss moduli of the experimental elastomer over a wide temperature range (25–165 °C), and we find that the elastomer remains stable and that the elastic character prevails (Fig. S7b). Moreover, this low-viscosity feature can also be verified by the cyclic tensile tests which show low hysteresis over three sequential loading-unloading cycles (Fig. S8).

Competition between photocuring and healing

The IBDA-enabled partial oxidation is an approach to regulate the photocuring and self-healing properties. Since the total concentration of thiol groups (c_{T0}) is

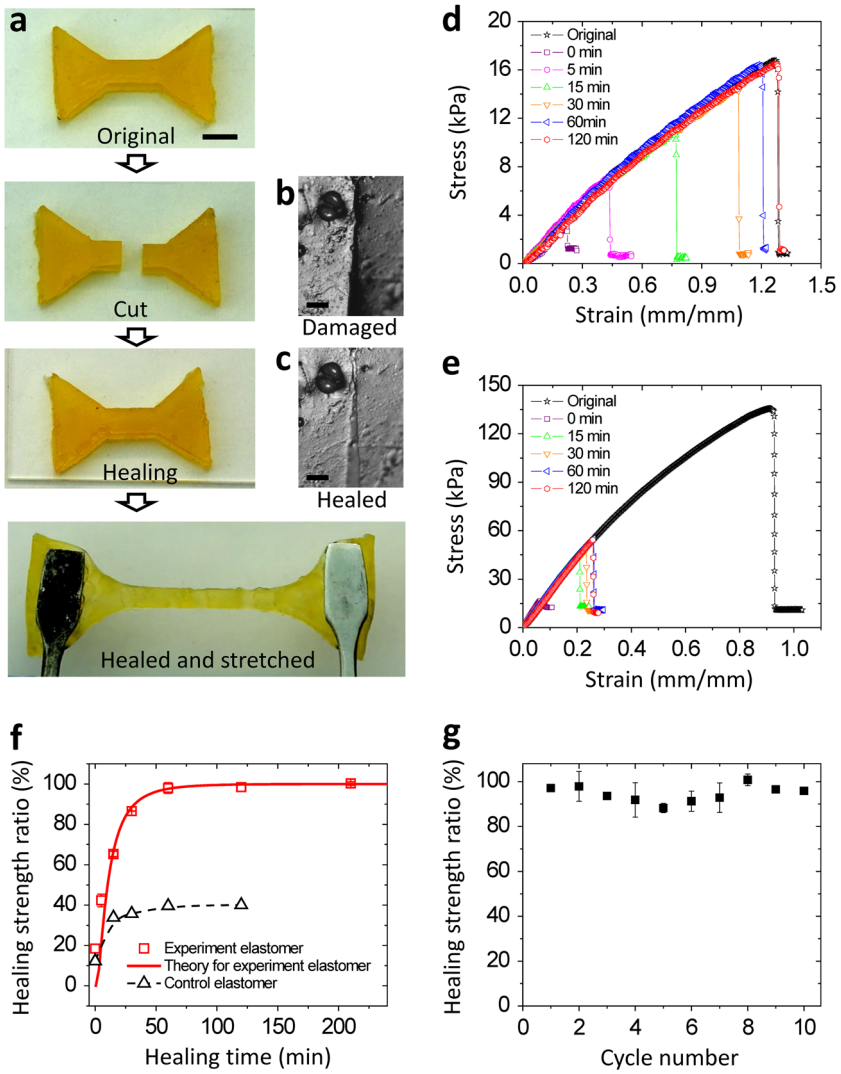

Fig. 2 Characterization of the self-healing property. a Self-healing process of a dog-bone-shaped elastomer sample. A dog-bone-shaped sample is first cut with a blade and brought into contact to heal for 2 h at 60 °C. The healed sample is then uniaxially stretched. The scale bar represents 5 mm. **b**, **c** The optical microscope images of the **b** damaged and **c** healed interfaces. The scale bars in (**b**, **c**) represent 50 μm. **d** Nominal stress-strain curves of the original and self-healed experimental elastomers for various healing times. The nominal stress is calculated as the force over the initial cross-section area of the sample neck. **e** Nominal stress-strain curves of the original and self-healed control elastomers for various healing times. **f** Healing strength ratios of the experimental and control elastomers as functions of the healing time at 60 °C. The healing strength ratio is defined as the healing strength of the self-healed sample over that of the original sample. The theoretically predicted relationship between the healing strength ratio and the healing time of the experimental elastomer agrees well with the experimental results. **g** Healing strength ratios of the experimental elastomers for 10-cycle healing tests (each 2 h at 60 °C)

initially provided, the concentrations of thiol (c_T) and disulfide groups (c_d) in the material ink are conserved ($c_T + 2c_d \approx c_{T0}$ if we assume the ink volume is approximately unchanged). The number of thiol group affects the photocuring rate, and the number of disulfide group influences the healing performance; therefore, the photocuring rate and the healing efficiency are expected to be competitive. This point can first be verified by the Raman spectroscopy measurements: the Raman peak associated with the disulfide bond becomes stronger as the IBDA concentration increases (Fig. 3a), indicating that disulfide bond concentration increases as more oxidant IBDA is applied. To further verify the competition, we carried out photocuring experiments to measure the relationship between the curing depth and the photoexposure time for various IBDA concentrations (Fig. 3b). We find that the curing depth H has an approximately linear relationship with the photoexposure time t, written as $H \approx k(t - t_0)$, where k is the curing coefficient (μm/s) and t_0 is the threshold time for the curing depth growth. The curing

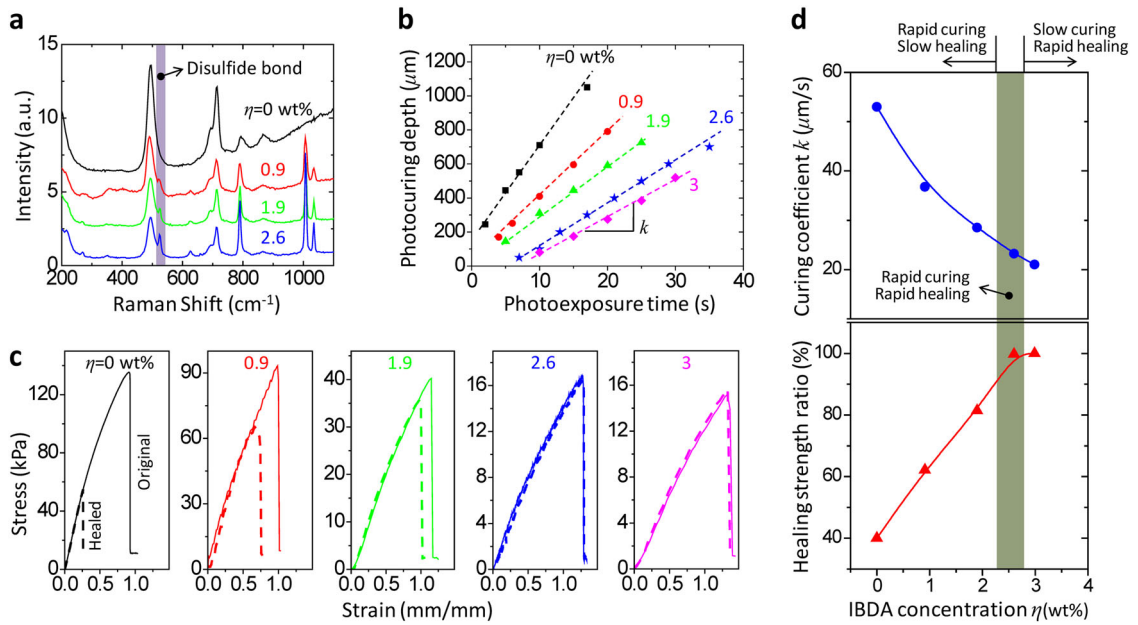

Fig. 3 Competition between the photocuring and self-healing. a Raman spectra of the elastomer ink with various IBDA concentrations η (wt%). The band at ~520 cm^{-1} corresponds to the disulfide bond. **b** Photocuring depth of the photoelastomer ink as a function of the photoexposure time for various IBDA concentrations. The slope is defined as the photocuring coefficient k (μm/s). **c** Nominal stress-strain curves of the original and self-healed elastomers (2-h healing at 60 °C) for various IBDA concentrations. **d** The photocuring coefficients and healing strength ratios (2-h healing at 60 °C) of the photoelastomer as functions of the applied IBDA concentration. The shadow region with IBDA concentration $\eta = 2.2–2.8$ wt% corresponds to rapid photocuring and rapid healing

coefficient k represents the photocuring rate during the AM process. The curing coefficient k decreases with increasing IBDA concentrations ($\eta = 0–3$ wt%) because more IBDAs transform more thiol groups to disulfide groups (Fig. 3b). At the same time, we find that the healing strength ratios of the cured elastomers within 2 h healing time (at 60 °C) increase as the IBDA concentration increases within $\eta = 0–2.6$ wt% (Fig. 3c). This result confirms that the properties of photocuring and self-healing are indeed competitive, and judicious selection of the IBDA concentration is required to enable both rapid photocuring and rapid self-healing. We further find that when the IBDA concentration is greater than $\eta_0 = 2.6$ wt %, the healing strength ratio reaches a plateau at 100% (Fig. 3d). To enable both rapid curing and rapid self-healing (> 90% within 2 h at 60 °C), we choose the IBDA concentration $\eta = 2.2–2.8$ wt% to carry out the oxidation experiments. If the IBDA concentration is out of this range, rapid photocuring and rapid healing cannot be achieved simultaneously.

Theoretical modeling of the self-healing behavior

To theoretically understand the self-healing behavior of photoelastomers, we develop a polymer-network-based model that is an extension of a model we recently developed for self-healing hydrogels crosslinked by nanoparticles[53] (model details in SI and Figs. S9-S13). The theory employs a bell-like model to analyze the stretching-induced dissociation of the dynamic disulfide bonds during the tensile loading process[54] and a diffusion-reaction model to capture the chain interpenetration and recrosslinking during the self-healing process[55–57]. Using this theoretical model, we can consistently explain the experimentally measured stress-strain behaviors of the original and self-healed samples (Fig. S13). The predicted healing strength ratios also agree well with the experiments (Fig. 2f). To further verify the theory, we carry out the self-healing experiments at various temperatures (40–60 °C). The experiments show that a higher temperature leads to a more rapid healing process. Our theory can also consistently explain the experimentally measured relationships between the healing strength ratios and healing time for various temperatures (Fig. S13c). It is worth noting that the temperature plays a key role during the self-healing process. As identified from the theoretical model, the self-healing capability of the designed photoelastomer is governed by the polymer chain diffusion and disulfide group-enabled reaction across the fractured interface. A higher temperature enables the more rapid diffusion of polymer chains across the fractured interface. Additionally, according to Bell's theory[54], increasing the temperature will increase the vibrational excitation of the sulfide atoms and favor the reformation of disulfide bonds during

the self-healing process. Both of these aspects have been well captured in our theoretical model. We expect that this theoretical framework can be further extended to understand self-healing soft polymers with various dynamic bonds, including dynamic covalent bonds[6,7], hydrogen bonds[8–10], metal-ligand coordination[11,12], and ionic interactions[14,15].

Applications of additively manufactured self-healing elastomers

Self-healable 3D soft actuator

To demonstrate potential applications, we first present a self-healable 3D soft actuator (Fig. 4a–c). The actuator is composed of a series of circular cones that can be shrunk inward to enable a contraction when a negative pressure is applied (Fig. 4a, the experimental setup in Fig. S14). When a negative pressure 30 kPa is applied, the actuator (~1 g) can lift a 10 g weight (~10 times its own weight) a distance of 6 mm. Then, we cut the actuator into two parts and bring them into contact to heal for 2 h at 60 °C. Once the actuator is self-healed, it can lift the 10 g weight a distance 6 mm again (Fig. 4a, b). The pressure-distance curve of the healed sample is very similar to that of the original one (Fig. 4c). This lifting efficiency (lifting weight per self-weight) is comparable with existing contraction actuators that are fabricated with molding or assembly methods[19,58]. Compared with the soft actuators fabricated using the traditional molding method[21,25], the stereolithography-enabled fabrication of the self-healable soft actuator requires less time and material consumption. Compared with the AM-enabled soft actuators composed of nonhealable materials[59,60], this soft actuator harnesses the self-healing elastomers to enable 100% healing after fatal fractures.

Self-healable structural composite

Natural structural materials, such as nacres and teeth, feature outstanding toughness, primarily due to their multiphase composition in which both stiff and soft phases are arranged in complex architectures[26,27]. These structural composites motivate tremendous efforts in creating tough synthetic composites with multiple phases[26,27]; however, these natural and synthetic composites are generally not self-healable. Here, we demonstrate AM of a healable nacre-like composite composed of a nonhealable stiff plastic phase and a healable soft elastomer phase (Fig. 4d, the multimaterial stereolithography system is shown in Fig. S15). During the photopolymerization enabled AM process, a thiol-acrylate reaction is triggered to enable a relatively strong interfacial bonding between the two phases (Fig. S16a)[61]. Under a tensile load, the crack in the composite sample (with a small crack notch) propagates through the soft phase in a wavy pattern, inducing a greater toughness than the parent materials (Fig. 4e and S16b). Since the crack propagates through the soft phase, we bring the two fractured parts back to heal for 2 h at 60 °C. After the healing process, the sample can sustain the tensile load again, and the toughness is ~90% of that of the original composite (Fig. 4d, e). As a control experiment, we manufacture a stiff-soft composite with nonhealable soft elastomers that only shows 14.5% of the original toughness in the second load (Fig. 4e and S16c).

Self-healable architected electronics

The self-healing photoelastomer is dielectric; to enable electronic conductivity, we dope carbon-blacks into the elastomer ink (Fig. 4f, see Methods). We additively manufacture a flexible composite pad with a dielectric elastomer phase and a conductive elastomer phase with a contour path of the USC Trojan. We show that the sample is conductive along the Trojan path to power an LED, and can also be bent at a large angle (~120°). Since both phases in the composite pad are self-healable, we then bring two parts back to heal the interface for 4 h at 60 °C. The healed pad becomes conductive again and can be used to power the LED. We find that the resistance of the healed sample only changes by 9% (Fig. 4g). The composite pad can be used as a self-healable force sensor, as the resistance of the conductive pathway decreases with an increase in the compressive force (Fig. 4h). This result is likely due to the effective spacing between carbon black particles within the conductor becoming smaller when a compressive force is applied[16]. The relationship between the relative resistance and the applied force can be used as a sensing signal to inversely predict the applied force. When we cut the structure and heal back for 4 h at 60 °C, we obtain a self-healed force sensor with the resistance-force curve close to that of the original force sensor (Fig. 4h).

Discussion

In summary, we present a molecularly designed photoelastomer ink that can enable stereolithography-based AM of elastomers with rapid and full self-healing. The dual functions of photopolymerization and self-healing are achieved by molecularly balancing the thiol and disulfide groups in the material ink. As a model self-healing photoelastomer, the material system with adequate modifications should be easily translatable to other photopolymerization-based AM systems, such as self-propagation photopolymer waveguide[37,38], two-photon lithography[39,40,62], and PolyJet printing[41]. The AM of self-healing elastomers with various tailored 3D architectures is expected to open various application possibilities not limited to the demonstrated 3D soft actuators (Fig. 4a–c), structural composites (Fig. 4d, e), and flexible electronics (Fig. 4f–h) but may also include artificial organs, biomedical implants, and bionic sensors and

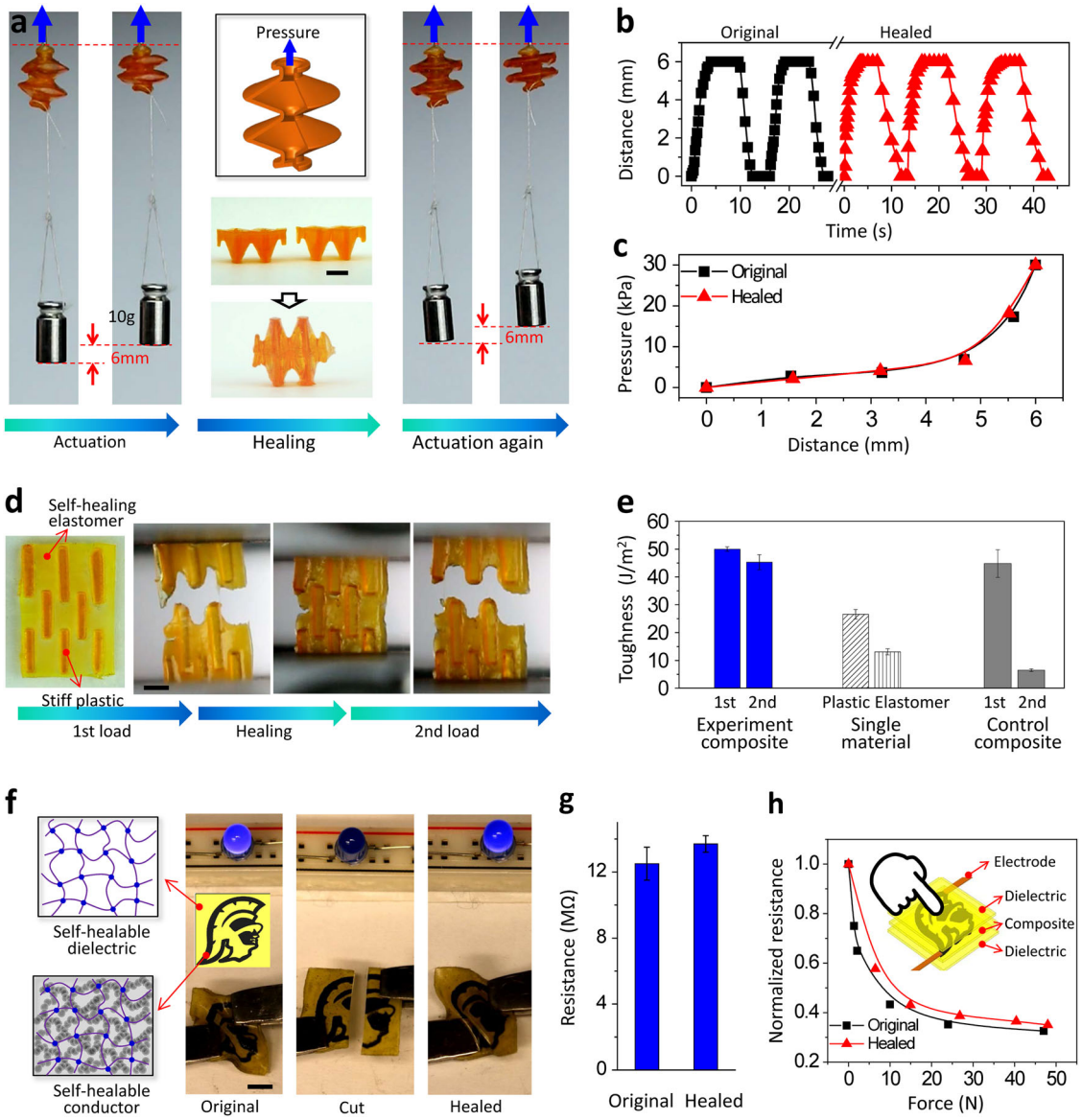

Fig. 4 Applications of additively manufactured self-healing elastomers. a–c Self-healable 3D soft actuator. **a** Negative pressure actuation can enable the additively manufactured elastomer actuator to lift a 10 g weight by 6 mm. The inset shows the CAD model of the elastomer actuator. The actuator is then cut in half and brought into contact to heal for 2 h at 60 °C. The self-healed actuator can be actuated again by the negative pressure to lift the 10 g weight by 6 mm. The scale bar represents 5 mm. **b** The cyclic lifting distance of the 10 g weight as a function of time of the original and self-healed actuators. **c** The relationships between the negative pressure values and the lifting distances of the original and self-healed actuators. **d**, **e** Self-healable structural composite. **d** A notched stiff-soft composite is first uniaxially stretched until a rupture and then brought into contact to heal for 2 h at 60 °C. The healed composite is then uniaxially stretched again until a rupture. The scale bar represents 3 mm. **e** The toughnesses of the original and healed experimental composites, single materials (pure plastic and pure elastomer), and the original and healed control composites. The toughness is defined as the enveloped area of the uniaxial nominal stress-strain curves until the rupture per unit sample area. **f–h** Self-healable architected electronics. **f** A flexible Trojan pad with a self-healable elastomer phase and a self-healable conductor phase can power an LED. Once cut and healed after 4 h at 60 °C, the self-healed Trojan pad can again sustain bending and power the LED. The scale bar represents 4 mm. **g** The resistance of the conductive path of the Trojan path before and after self-healing. **h** The relationships between the normalized resistances and the applied force of the original and self-healed force sensors. The normalized resistance is calculated as the resistance normalized by the resistance for the force-free state. The inset shows the working paradigm of the force sensor

robotics[20,25,42,63,64]. In addition, in nature, the disulfide bond is a reversible cross-link that provides tunable stability to folded structures of proteins with specific mechanical functions, such as molecular sensing, switching, and signaling[65,66]. The AM of biomimetic materials with dynamic disulfide bonds may open

possibilities for materials with protein-like functions. Moreover, as a model system to incorporate desirable material properties (i.e., self-healing) into the existing AM system, the molecular design strategy may be extended to various other salient properties, such as stimulus actuation[41,67] and mechanochromism[68]. To that end, the presented strategy may motivate molecular designs of various unprecedented material inks for emerging AM systems to enable rapid prototyping of 3D structures that cannot be fabricated with traditional shaping methods[38,69–71].

Acknowledgements
The authors acknowledge funding support from the Air Force Office of Scientific Research Young Investigator Program (FA9550-18-1-0192, Program Manager: Dr. Jaimie S. Tiley) and the National Science Foundation (CMMI-1762567). The authors thank Dr. Qibing Pei at the University of California, Los Angeles, for using the RSA III TA instrument.

Author contribution
K.Y. and Q.W. designed the research, developed the analytical models, and interpreted the results. K.Y. carried out the experiments with the technical support of A.X.. H.D., K.Y., and Q.W. wrote the manuscript, and all authors contributed to revising the manuscript.

Conflict of interest
The University of Southern California has filed a patent application related to the work described here.

Publisher's note
Springer Nature remains neutral with regard to jurisdictional claims in published maps and institutional affiliations.

Supplementary information is available for this paper at https://doi.org/10.1038/s41427-019-0109-y.

Received: 13 September 2018 Revised: 21 November 2018 Accepted: 16 December 2018
Published online: 01 February 2019

References

1. Wu, D. Y., Meure, S. & Solomon, D. Self-healing polymeric materials: a review of recent developments. *Progress. Polym. Sci.* **33**, 479–522 (2008).
2. Blaiszik, B. et al. Self-healing polymers and composites. *Annu. Rev. Mater. Res.* **40**, 179–211 (2010).
3. Yang, Y. & Urban, M. W. Self-healing polymeric materials. *Chem. Soc. Rev.* **42**, 7446–7467 (2013).
4. Toohey, K. S., Sottos, N. R., Lewis, J. A., Moore, J. S. & White, S. R. Self-healing materials with microvascular networks. *Nat. Mater.* **6**, 581–585 (2007).
5. White, S. R. et al. Autonomic healing of polymer composites. *Nature* **409**, 794–797 (2001).
6. Chen, X. et al. A thermally re-mendable cross-linked polymeric material. *Science* **295**, 1698–1702 (2002).
7. Ghosh, B. & Urban, M. W. Self-repairing oxetane-substituted chitosan polyurethane networks. *Science* **323**, 1458–1460 (2009).
8. Sijbesma, R. P. et al. Reversible polymers formed from self-complementary monomers using quadruple hydrogen bonding. *Science* **278**, 1601–1604 (1997).
9. Cordier, P., Tournilhac, F., Soulié-Ziakovic, C. & Leibler, L. Self-healing and thermoreversible rubber from supramolecular assembly. *Nature* **451**, 977–980 (2008).
10. Chen, Y., Kushner, A. M., Williams, G. A. & Guan, Z. Multiphase design of autonomic self-healing thermoplastic elastomers. *Nat. Chem.* **4**, 467–472 (2012).
11. Burnworth, M. et al. Optically healable supramolecular polymers. *Nature* **472**, 334–337 (2011).
12. Li, C.-H. et al. A highly stretchable autonomous self-healing elastomer. *Nat. Chem.* **8**, 618 (2016).
13. Okay O. Self-healing hydrogels formed via hydrophobic interactions. In: Supramolecular Polymer Networks and Gels (ed Seiffert S). Springer (2015). https://link.springer.com/chapter/10.1007/978-3-319-15404-6_3.
14. Wang, Q. et al. High-water-content mouldable hydrogels by mixing clay and a dendritic molecular binder. *Nature* **463**, 339–343 (2010).
15. Sun, T. L. et al. Physical hydrogels composed of polyampholytes demonstrate high toughness and viscoelasticity. *Nat. Mater.* **12**, 932–937 (2013).
16. Tee, B. C., Wang, C., Allen, R. & Bao, Z. An electrically and mechanically self-healing composite with pressure-and flexion-sensitive properties for electronic skin applications. *Nat. Nanotechnol.* **7**, 825–832 (2012).
17. Zou, Z. et al. Rehealable, fully recyclable, and malleable electronic skin enabled by dynamic covalent thermoset nanocomposite. *Sci. Adv.* **4**, eaaq0508 (2018).
18. Oh, J. Y. et al. Intrinsically stretchable and healable semiconducting polymer for organic transistors. *Nature* **539**, 411 (2016).
19. Acome, E. et al. Hydraulically amplified self-healing electrostatic actuators with muscle-like performance. *Science* **359**, 61–65 (2018).
20. Bilodeau, R. A. & Kramer, R. K. Self-healing and damage resilience for soft robotics: a review. *Front. Robot. AI* **4**, 48 (2017).
21. Terryn, S., Brancart, J., Lefeber, D., Van Assche, G. & Vanderborght, B. Self-healing soft pneumatic robots. *Sci. Robot.* **2**, eaan4268 (2017).
22. Wang, C. et al. Self-healing chemistry enables the stable operation of silicon microparticle anodes for high-energy lithium-ion batteries. *Nat. Chem.* **5**, 1042–1048 (2013).
23. Zaribaf, B. H., Lee, S.-J., Kim, J.-H., Park, P.-K. & Kim, J.-H. Toward in situ healing of compromised polymericmembranes. *Environ. Sci. Technol. Lett.* **1**, 113–116 (2014).
24. Brochu, A. B., Craig, S. L. & Reichert, W. M. Self-healing biomaterials. *J. Biomed. Mater. Res. A.* **96**, 492–506 (2011).
25. Rus, D. & Tolley, M. T. Design, fabrication and control of soft robots. *Nature* **521**, 467 (2015).
26. Studart, A. R. Additive manufacturing of biologically-inspired materials. *Chem. Soc. Rev.* **45**, 359–376 (2016).
27. Wegst, U. G., Bai, H., Saiz, E., Tomsia, A. P. & Ritchie, R. O. Bioinspired structural materials. *Nat. Mater.* **14**, 23–36 (2015).
28. Benight, S. J., Wang, C., Tok, J. B. & Bao, Z. Stretchable and self-healing polymers and devices for electronic skin. *Progress. Polym. Sci.* **38**, 1961–1977 (2013).
29. Liu, S. & Li, L. Ultrastretchable and Self-Healing Double-Network Hydrogel for 3D Printing and Strain Sensor. *ACS Appl. Mater. & Interfaces* **9**, 26429–26437 (2017).
30. Darabi, M. A. et al. Skin-inspired multifunctional autonomic-intrinsic conductive self-healing hydrogels with pressure sensitivity, stretchability, and 3D printability. *Adv. Mater.* **29**, 1700533 (2017).
31. Nadgorny, M., Xiao, Z. & Connal, L. A. 2D and 3D-printing of self-healing gels: design and extrusion of self-rolling objects. *Mol. Syst. Des. Eng.* **2**, 283–292 (2017).
32. Kuang, X. et al. 3D printing of highly stretchable, shape-memory, and self-healing elastomer toward novel 4D printing. *ACS Appl. Mater. Interfaces* **10**, 7381–7388 (2018).
33. Bhattacharjee, T. et al. Writing in the granular gel medium. *Sci. Adv.* **1**, e1500655 (2015).
34. Moderator:, Trimmer, B., Participants:, Lewis, J. A., Shepherd, R. F. & Lipson, H. 3D printing soft materials: what is possible? *Soft Robot.* **2**, 3–6 (2015).
35. Zheng, X. et al. Ultralight, ultrastiff mechanical metamaterials. *Science* **344**, 1373–1377 (2014).
36. Wang, Q. et al. Lightweight mechanical metamaterials with tunable negative thermal expansion. *Phys. Rev. Lett.* **117**, 175901 (2016).
37. Schaedler, T. A. et al. Ultralight metallic microlattices. *Science* **334**, 962–965 (2011).
38. Eckel, Z. C. et al. Additive manufacturing of polymer-derived ceramics. *Science* **351**, 58–62 (2016).
39. Meza, L. R., Das, S. & Greer, J. R. Strong, lightweight, and recoverable three-dimensional ceramic nanolattices. *Science* **345**, 1322–1326 (2014).
40. Bauer, J., Schroer, A., Schwaiger, R. & Kraft, O. Approaching theoretical strength in glassy carbon nanolattices. *Nat. Mater.* **15**, 438–443 (2016).
41. Ding, Z. et al. Direct 4D printing via active composite materials. *Sci. Adv.* **3**, e1602890 (2017).
42. Truby, R. L. & Lewis, J. A. Printing soft matter in three dimensions. *Nature* **540**, 371 (2016).
43. Tumbleston, J. R. et al. Continuous liquid interface production of 3D objects. *Science* **347**, 1349–1352 (2015).

44. Zhou, J., Zhang, Q., Zhang, H., Tan, J. & Chen, S. Evaluation of thiol-ene photocurable resins using in rapid prototyping. *Rapid Prototyp. J.* **22**, 465–473 (2016).
45. Lei, Z. Q., Xiang, H. P., Yuan, Y. J., Rong, M. Z. & Zhang, M. Q. Room-temperature self-healable and remoldable cross-linked polymer based on the dynamic exchange of disulfide bonds. *Chem. Mater.* **26**, 2038–2046 (2014).
46. Rattanangkool, E. et al. Hypervalent Iodine (III)-promoted metal-free S–H activation: an approach for the construction of S–S, S–N, and S–C bonds. *Eur. J. Org. Chem.* **2014**, 4795–4804 (2014).
47. Acosta Ortiz R., et al. Self-Healing Photocurable Epoxy/thiol-ene Systems Using an Aromatic Epoxy Resin. *Adv. Mater. Sci. Eng.* **2016**, 8245972 (2016). https://www.hindawi.com/journals/amse/2016/8245972/.
48. Nguyen, K. D., Megone, W. V., Kong, D. & Gautrot, J. E. Ultrafast diffusion-controlled thiol–ene based crosslinking of silicone elastomers with tailored mechanical properties for biomedical applications. *Polym. Chem.* **7**, 5281–5293 (2016).
49. Wallin, T. et al. Click chemistry stereolithography for soft robots that self-heal. *J. Mater. Chem. B* **5**, 6249–6255 (2017).
50. Xu, Y. & Chen, D. A novel self-healing polyurethane based on disulfide bonds. *Macromol. Chem. Phys.* **217**, 1191–1196 (2016).
51. Jian, X., Hu, Y., Zhou, W. & Xiao, L. Self-healing polyurethane based on disulfide bond and hydrogen bond. *Polym. Adv. Technol.* **29**, 463–469 (2018).
52. Wool, R. P. Self-healing materials: a review. *Soft Matter* **4**, 400–418 (2008).
53. Wang, Q., Gao, Z. & Yu, K. Interfacial self-healing of nanocomposite hydrogels: theory and experiment. *J. Mech. Phys. Solids* **109**, 288–306 (2017).
54. Bell, G. I. Models for the specific adhesion of cells to cells. *Science* **200**, 618–627 (1978).
55. de Gennes, P. G. Reptation of a polymer chain in the presence of fixed obstacles. *J. Chem. Phys.* **55**, 572–579 (1971).
56. Rubinstein M., Colby R. *Polymer Physics*. (Oxford University Press, Oxford, 2003).
57. Crank J. *The mathematics of diffusion*. (Oxford university press, Oxford, 1979).
58. Yang, D. et al. Buckling pneumatic linear actuators inspired by muscle. *Adv. Mater. Technol.* **1**, 1600055 (2016).
59. Wehner, M. et al. An integrated design and fabrication strategy for entirely soft, autonomous robots. *Nature* **536**, 451 (2016).
60. Schaffner, M. et al. 3D printing of robotic soft actuators with programmable bioinspired architectures. *Nat. Commun.* **9**, 878 (2018).
61. Jian, Y. et al. Thiol–epoxy/thiol–acrylate hybrid materials synthesized by photopolymerization. *J. Mater. Chem. C.* **1**, 4481–4489 (2013).
62. Bauer, J. et al. Nanolattices: an emerging class of mechanical metamaterials. *Adv. Mater.* **29**, 1701850 (2017).
63. Melchels, F. P. et al. Additive manufacturing of tissues and organs. *Progress. Polym. Sci.* **37**, 1079–1104 (2012).
64. Kong, Y. L., Gupta, M. K., Johnson, B. N. & McAlpine, M. C. 3D printed bionic nanodevices. *Nano Today* **11**, 330–350 (2016).
65. Åslund, F. & Beckwith, J. Bridge over troubled waters. *Cell* **96**, 751–753 (1999).
66. Hogg, P. J. Disulfide bonds as switches for protein function. *Trends Biochem. Sci.* **28**, 210–214 (2003).
67. Gladman, A. S., Matsumoto, E. A., Nuzzo, R. G., Mahadevan, L. & Lewis, J. A. Biomimetic 4D printing. *Nat. Mater.* **15**, 413 (2016).
68. Wang, Q., Gossweiler, G. R., Craig, S. L. & Zhao, X. Cephalopod-inspired design of electro-mechano-chemically responsive elastomers for on-demand fluorescent patterning. *Nat. Commun.* **5**, 4899 (2014).
69. Hegde, M. et al. 3D printing all-aromatic polyimides using mask-projection stereolithography: processing the nonprocessable. *Adv. Mater.* **29**, 1701240 (2017).
70. Vyatskikh, A. et al. Additive manufacturing of 3D nano-architected metals. *Nat. Commun.* **9**, 593 (2018).
71. Zhang, B., Kowsari, K., Serjouei, A., Dunn, M. L. & Ge, Q. Reprocessable thermosets for sustainable three-dimensional printing. *Nat. Commun.* **9**, 1831 (2018).

Supplementary Information for
Additive Manufacturing of Self-Healing Elastomers

Kunhao Yu[1], An Xin[1], Haixu Du[1], Ying Li[2], Qiming Wang[1*]

[1]Sonny Astani Department of Civil and Environmental Engineering, University of Southern California, Los Angeles, CA 90089, USA
[2]Department of Mechanical Engineering and Institute of Materials Science, University of Connecticut, Storrs, CT 06269, USA
*Email: qimingw@usc.edu

1. Supplementary method: analytical modeling of disulfide-bond enabled self-healing

We develop a polymer-network based model to explain the experimentally measured self-healing behaviors of the created elastomer with disulfide bonds. This model is an extension of a model we recently developed for self-healing hydrogels crosslinked by nanoparticles[1]. We first model the constitutive behavior of the original elastomer and then model the interfacial self-healing behavior of the fractured elastomer.

1.1. Constitutive modeling of original elastomer

We assume that the elastomer is composed of *m* types of networks interpenetrating in the material bulk space (**Fig. S9**)[2]. The *i*th network is composed of the *i*th polymer chains with n_i Kuhn segment number. The length of the *i*th chain at the freely joint state is determined by the Kuhn segment number n_i as $r_i^0 = \sqrt{n_i}b$, where *b* is the Kuhn Segment length. Researchers usually denote the "chain length" as n_i[3]. Without loss of generality, the Kuhn segment number follows an order $n_1 \le n_2 ..... \le n_m$. We denote the number of *i*th chain per unit volume of material as N_i. Therefore, the total chain number per unit volume of material is $N = \sum_{i=1}^{m} N_i$. The chain number follows a statistical distribution as

$$P_i(n_i) = \frac{N_i}{N} \tag{S1}$$

The summation of the statistical distribution function is a unit, i.e., $\sum_{i=1}^{m} P_i = 1$. The chain-length distribution $P_i(n_i)$ is usually unknown without a careful experimental examination. Although researchers usually accept that the chain length is generally non-uniform[4], the most prevailing models for the rubber elasticity still consider the uniform chain length, such as three-chain model, four-chain model, and eight-chain model[3, 5, 6]. The consideration of non-uniform chain-length to model the elasticity behaviors of rubber-like materials was recently carried out by Wang et al. [2] and Vernerey et al.[7]. Because of the limited experimental technique to characterize the chain length distribution to date, the selection of chain-length distribution is still a little ambiguous. Wang et al. tested a number of chain-length distribution functions including uniform, Weibull, normal, and log-normal, and found that the log-normal distribution can best match the material's mechanical and mechanochemical behaviors [2]. In this paper, we simply employ the log-normal chain-length distribution, while other distributions may also work for our model. The log-normal chain-length distribution is written as

$$P_i(n_i) = \frac{1}{n_i \delta \sqrt{2\pi}} \exp\left[-\frac{(\ln n_i - \ln n_a)^2}{2\delta^2} \right] \tag{S2}$$

where n_a and δ are the mean of n_i and standard deviation of $\ln n_i$, respectively.

For the *i*th chain, if the end-to-end distance at the deformed state is r_i, the chain stretch is defined as $\Lambda_i = r_i / r_i^0$. The free energy of the deformed *i*th chain can be written as

$$w_i = n_i k_B T \left(\frac{\beta_i}{\tanh \beta_i} + \ln \frac{\beta_i}{\sinh \beta_i} \right) \tag{S3}$$

where k_B is the Boltzmann constant, T is the temperature in Kelvin, $\beta_i = L^{-1}\left(\Lambda_i / \sqrt{n_i}\right)$ and $L^{-1}(\ )$ is the inverse Langevin function. Considering the chain as an entropic spring, the force within the deformed *i*th chain can be written as

$$f_i = \frac{\partial w_i}{\partial r_i} = \frac{k_B T}{b} \beta_i \tag{S4}$$

To link the relationship between the macroscopic deformation at the material level and the microscopic deformation at the polymer chain level, we consider an interpenetrating model shown in **Fig. S9** [2]. We assume the *i*th chains assemble themselves into regular eight-chain structures[5]. We assume the material follows an affined deformation model[3, 6], so that the eight-chain structures deform by three principal stretches ($\lambda_1, \lambda_2, \lambda_3$) under the macroscopic deformation ($\lambda_1, \lambda_2, \lambda_3$) at the material level. Therefore, the stretch of each *i*th chain is

$$\Lambda_i = \sqrt{\frac{\lambda_1^2 + \lambda_2^2 + \lambda_3^2}{3}} \tag{S5}$$

At the undeformed state, the number of the *i*th chain per unit material volume is N_i. As the material is deformed, the active *i*th chain number decreases because the chain force promotes the dissociation of the dynamic bonds. We assume at the deformed state, the number of the active *i*th chain per unit material volume is N_i^a. Since every *i*th chain undergoes the same stretch Λ_i, the total free energy of the material per unit volume is

$$W = \sum_{i=1}^{m} N_i^a n_i k_B T \left(\frac{\beta_i}{\tanh \beta_i} + \ln \frac{\beta_i}{\sinh \beta_i} \right) \tag{S6}$$

where $\beta_i = L^{-1}\left(\Lambda_i / \sqrt{n_i}\right)$ and Λ_i is given in **Eq. S9**, and the active *i*th chain density N_i^a is obtained in the following sections.

We consider the material as incompressible and it is uniaxially stretched with three principal stretches ($\lambda_1 = \lambda, \lambda_2 = \lambda_3 = \lambda^{-1/2}$), the nominal stress along λ_1 direction can be calculated as

$$s_1 = \frac{\left(\lambda - \lambda^{-2}\right) k_B T}{\sqrt{3\lambda^2 + 6\lambda^{-1}}} \sum_{i=1}^{m} \left[N_i^a \sqrt{n_i} L^{-1}\left(\sqrt{\frac{\lambda^2 + 2\lambda^{-1}}{3n_i}} \right) \right] \tag{S7}$$

Next, we consider the association-dissociation kinetics of dynamic disulfide bonds (**Fig. S10**). We model the bond association and dissociation as a reversible chemical reaction[8, 9]. The forward reaction rate (from the associated state to the dissociated state) is k_i^f and reverse reaction rate is k_i^r. For simplicity, we assume that only two ends of a chain have ending groups for the dynamic bond [10]. If two end groups are associated, we consider this chain as "active"; otherwise, the chain is "inactive". The chemical reaction in **Fig. S10a** averagely involves one polymer chain; that is, the chemical reaction represents the transition between an active chain and an inactive chain. Here we denote the active *i*th chain per unit volume is N_i^a and the inactive *i*th chain per unit volume is N_i^d. The chemical kinetics can be written as

$$\frac{dN_i^a}{dt} = -k_i^f N_i^a + k_i^r N_i^d \tag{S8}$$

Since the total number of *i*th chain per unit volume defined as $N_i = N_i^a + N_i^d$, the chemical kinetics can be rewritten as

$$\frac{dN_i^a}{dt} = -\left(k_i^f + k_i^r\right) N_i^a + k_i^r N_i \tag{S9}$$

At the as-fabricated undeformed state, the reaction rates are $k_i^f = k_i^{f0}$ and $k_i^r = k_i^{r0}$, respectively. As the material is fabricated as an integrated solid, we simply assume the association reaction is much stronger than the dissociation reaction at the fabricated state, i.e., $k_i^{f0} \ll k_i^{r0}$. Otherwise, the polymer is unstable under external perturbations. Therefore, most of the *i*th chains are at the associated state, as the equilibrium value of N_i^a at the undeformed state is

$$N_i^a = \frac{k_i^{r0}}{k_i^{r0} + k_i^{f0}} N_i \approx N_i \tag{S10}$$

At the deformed state, the *i*th chain is deformed with stretch Λ_i. Since the bond strength of the dynamic bonds is much weaker than those of the permanent bonds such as covalent bonds, the chain force would significantly alter the bonding reaction [8, 9]. Specifically, the chain force tends to pull the bond open to the dissociated state. This point has been well characterized by Bell model for the ligand-receptor bonding for the cell adhesion behaviors, as well as for biopolymers [11]. We here employ a Bell-like model and consider the energy landscape between the associated state and dissociated state shown in **Fig. S10bc** [2]. We consider an energy barrier exists between the associated state (denoted as "A") and the dissociated state ("D") through a transition state ("T"). At the undeformed state of the *i*th chain, the energy barrier for $\mathrm{A} \to \mathrm{D}$ transition is ΔG^f and the energy barrier for $\mathrm{D} \to \mathrm{A}$ transition is ΔG^r (**Fig. S10b**). Under the deformed state of the *i*th chain, the chain force f_i lowers down the energy barrier of $\mathrm{A} \to \mathrm{D}$ transition to $\Delta G^f - f_i \Delta x$ and increases the energy barrier for $\mathrm{D} \to \mathrm{A}$ transition to $\Delta G^r + f_i \Delta x$, where Δx is the distance along the energy landscape coordinate (**Fig. S10c**). Since the occurrence of the chemical reaction

requires the overcoming of the energy barriers, the higher energy barrier is corresponding to the lower likelihood of the reaction. According to the Bell model, the reaction rates are governed by the energy barrier through exponential functions as [11, 12].

$$k_i^f = C_1 \exp\left(-\frac{\Delta G^f - f_i \Delta x}{k_B T}\right) = k_i^{f0} \exp\left(\frac{f_i \Delta x}{k_B T}\right) \tag{S11a}$$

$$k_i^r = C_2 \exp\left(-\frac{\Delta G^r + f_i \Delta x}{k_B T}\right) = k_i^{r0} \exp\left(-\frac{f_i \Delta x}{k_B T}\right) \tag{S11b}$$

Where C_1 and C_2 are constants and Δx is treated as a fitting parameter for the given material.

If the material is loaded with increasing stretch ($\lambda_1 = \lambda, \lambda_2 = \lambda_3 = \lambda^{-1/2}$) with a very small loading rate, the deformation of the material is assumed as quasi-static. It means that in every small increment of the load, the chemical reaction already reaches its equilibrium state with an equilibrium active *i*th chain number N_i^a. Under this condition, the active *i*th chain number per unit material volume is expressed as

$$N_i^a = \frac{N_i k_i^{r0} \exp\left(-\frac{f_i \Delta x}{k_B T}\right)}{k_i^{f0} \exp\left(\frac{f_i \Delta x}{k_B T}\right) + k_i^{r0} \exp\left(-\frac{f_i \Delta x}{k_B T}\right)} \tag{S12}$$

with the chain force f_i as expressed in **Eq. S4**.

In addition to the above association-dissociation kinetics, we also consider the effect of the network alteration[13, 14]. During the mechanical loading, a portion of dissociated short chains may reorganize to become active long chains[13, 14]. To capture this effect, we follow the network alteration theory to model the number of active chains to be an exponential function of the chain stretch Λ_i as

$$\frac{N_i^a}{N_i} = \exp\left[\alpha(\Lambda_i - 1)\right] \tag{S13}$$

where α is the chain alteration parameter. Similar network alteration model has been employed to model the chain reorganization for the Mullin's effect of rubber [13, 14], double-network hydrogels [15], and nanocomposite hydrogels [16]. It has been shown that the network alteration is a unique network damage mechanism that facilitates the stiffening effect of the stress-stretch curve [13, 14, 16]. Here, we harness this network alteration effect to better capture the stress-stretch curve shapes of the original elastomer.

1.2. Self-healing behavior of the fractured elastomer

We consider a self-healing elastomer sample shown in **Fig. S11**. We cut the sample into two parts and then immediately contact back. After a certain period of healing time *t*, the sample is uniaxially stretched until rupturing into two parts again. Here, we consider the self-healed sample is composed of two segments (**Fig. S11**): Around the healing interface, the polymer chain would diffuse across the interface to form new networks through forming new dynamic bonds. We call this region as "self-healed

segment". Away from the self-healed segment, the polymer networks are intact, and we call this region as "virgin segment".

As we assume in section 1.1, the *i*th chains form network following eight-chain structures (**Fig. S9**). For simplicity of analysis, we assume the cutting position is located at a quarter part of the eight chain cube, namely the center position between a corner and the center of the eight-chain cube (**Fig. S12a**). This assumption is just for the sake of symmetry to enable easy analysis. Other anti-symmetry cutting positions can also be analyzed using an averaging concept. The cutting process forces the polymer chains to be dissociated from the dynamic bond around the corner or center positions. Since we immediately contact the material back, we assume the ending groups of the dynamic bonds are still located around the cutting interface, yet without enough time to migrate into the material matrix (**Fig. S12b**)[1]. Driven by weak interactions between ending groups of the dynamic bonds, the ending groups on the interface will diffuse across the interface to penetrate into the matrix of the other part of the material to form new dynamic bonds. Specifically shown in **Fig. S12b**, the ending groups of the part A will penetrate into part B towards the center position of the cube, and the ending groups of part B will penetrate into Part A towards the corner positions of the cube. These interpenetration behaviors can be simplified as a 1D model shown in **Fig. S12c**. As shown in **Fig. S12c**, an open ending group around the interface penetrates into the other part of the material to find another open ending group to form a dynamic bond. Once the dynamic bond reforms, the initially "inactive" chain becomes "active". This behavior can be understood as two processes: chain diffusion and ending group reaction.

In the disulfide bond system shown in **Fig. 1c**, when we cut the material into two parts, the dissociated sulfide bonds undergo disulfide metathesis reactions (assisted by a catalyst tributylphosphine) to reform disulfide bonds around the interface. When the two material parts are brought into contact, these disulfide bonds will be mobilized by the catalyst tributylphosphine to move across the interface to exchange sulfide groups to form disulfide bonds to bridge the interface. Our generalized model shown in **Fig. S12** and discussed above can approximately capture the key physics of the healing behaviors of the disulfide bond system.

To model the chain diffusion, we consider a reptation-like model shown in **Fig. S12c** [3, 17-19]. We assume the polymer chain diffuses along its contour tube analogous to the motion of a snake. The motion of the polymer chain is enabled by extending out small segments called "minor chains". The curvilinear motion of the polymer chain is characterized by the Rouse friction model with the curvilinear diffusion coefficient of the *i*th chain written as

$$D_i = \frac{k_B T}{n_i \xi} \tag{S14}$$

where ξ is the Rose friction coefficient per unit Kuhn segment.

We note that the chain motion follows a curvilinear path; therefore, we construct two coordinate systems *s* and *y*, where *s* denotes the curvilinear path along the minor chains and *y* denotes the linear path from the interface to the other open ending group. When the *i*th chain moves s_i distance along the curvilinear path, it is corresponding to y_i distance along *y* coordinate. Here we assume the selection of the

curvilinear path is fully stochastic following the Gaussian statistics[20-22]. Therefore, the conversion of the distances in two coordinate systems is expressed as

$$y_i = \sqrt{s_i b} \tag{S15}$$

According to the eight-chain cube assumption, the distance between the corner and the center within the *i*th network cube at its freely joint state is

$$L_i \approx \sqrt{n_i} b \tag{S16}$$

The distance between the ending group around the interface and the other ending group in the matrix is $L_i/2$. According to **Eq. S15**, the positions $y = 0$ and $y = L_i/2$ are corresponding to $s = 0$ and $s = L_i^2/4b$, respectively.

If we only consider the polymer chain diffusion, the diffusion of the *i*th chain can be modeled with the following diffusion equation along the curvilinear coordinate *s*,

$$\frac{\partial C_i^d(t,s)}{\partial t} = D_i \frac{\partial^2 C_i^d(t,s)}{\partial s^2} \tag{S17}$$

where $C_i^d(t,s)$ is the inactive *i*th chain number per unit length (with the unit area) along the coordinate *s* ($0 \le s \le L_i^2/4b$) at time *t*. However, the chain behavior is more complicated than just diffusion, because during the diffusion the ending group would encounter another ending group to undergo a chemical reaction to form a new dynamic bond. Although the chemical reaction may only occur around the ending group (relatively immobile ending group at $s = L_i^2/4b$), the reaction forms dynamic bonds to transit an inactive chain into an active chain, and this reaction would reduce the amount of the inactive ending groups and further drive the motion of the other inactive ending groups. Therefore, the chain diffusion and ending group reaction actually are strongly coupled. Therefore, we consider an effective diffusion-reaction model to consider the effective behaviors of the chain and the ending group as [23]

$$\frac{\partial C_i^d(t,s)}{\partial t} = D_i \frac{\partial^2 C_i^d(t,s)}{\partial s^2} - \frac{\partial C_i^a(t,s)}{\partial t} \tag{S18}$$

$$\frac{\partial C_i^a(t,s)}{\partial t} = k_i^{r0} C_i^d(t,s) - k_i^{f0} C_i^a(t,s) \tag{S19}$$

where $C_i^a(t,s)$ is the active *i*th chain number per unit length (with the unit area) along the coordinate *s* ($0 \le s \le L_i^2/4b$) at time *t*. As the polymer chain is freely joint during the diffusion process, we here use the chemical reaction rates k_i^{f0} and k_i^{r0}.

In the initial state of the self-healing, all mobile open-ending groups of the *i*th chains are located around the healing interface. Therefore, the initial condition of the diffusion-reaction model is

$$C_i^d(t=0,s) = N_i \delta(s) \tag{S20}$$

$$C_i^a(t=0,s)=0 \tag{S21}$$

where $\int_{-\infty}^{\infty}\delta(s)ds=1$.

For a self-healing polymer that is capable of forming a stable solid form and enabling relatively short healing time, the basic requirement is $k_i^{f0}<k_i^{r0}$. Here, we further focus our attention on polymers with good healing capability, so that the polymers can easily self-heal under relatively mild conditions. This requirement further implies that k_i^{r0} should be much larger than k_i^{f0}, i.e., $k_i^{r0}>>k_i^{f0}$. Under this condition, **Eqs. S18-S19** can be reduced as

$$\frac{\partial C_i^d(t,s)}{\partial t}=D_i\frac{\partial^2 C_i^d(t,s)}{\partial s^2}-k_i^{r0}C_i^d(t,s) \tag{S22}$$

At the same time, around the location $s=L_i^2/4b$, all open ending groups form dynamic bonds. This leads to the vanishing of inactive chains around the location $s=L_i^2/4b$, written as

$$C_i^d\left(t,s=L_i^2/4b\right)=0 \tag{S23}$$

Along with above initial and boundary conditions, the reaction-diffusion equation (**Eq. S22**) can be solved analytically or numerically. Once $C_i^d(t,s)$ in the diffusion-reaction model is solved, we can further obtain the active *i*th chain number per unit volume of the self-healing segment at healing time *t*, written as

$$\frac{N_i^h(t)}{N_i}=1-\frac{4b}{L_i^2}\int_0^{L_i^2/4b}\frac{C_i^d(t,s)}{N_i}ds \tag{S24}$$

where $N_i^h(t)$ is for the self-healed segment at the undeformed state ($\lambda_1=\lambda_2=\lambda_3=1$), and the superscript "*h*" denotes "healed".

At the deformed state, the active *i*th chain number in the self-healed segment decreases with the increasing stretch. If we consider a quasistatic load with principal stretches ($\lambda_1=\lambda^h,\lambda_2=\lambda_3=\left(\lambda^h\right)^{-1/2}$), the active *i*th chain number per unit volume of the self-healing segment can be calculated as

$$N_i^{ah}(t)=\frac{N_i^h(t)k_i^{r0}\exp\left(-\frac{f_i\Delta x}{k_BT}\right)}{k_i^{f0}\exp\left(\frac{f_i\Delta x}{k_BT}\right)+k_i^{r0}\exp\left(-\frac{f_i\Delta x}{k_BT}\right)} \tag{S25}$$

with the chain force expressed as

$$f_i = \frac{k_B T}{b} L^{-1}\left(\sqrt{\frac{\left(\lambda^h\right)^2 + 2\left(\lambda^h\right)^{-1}}{3n_i}}\right) \tag{S26}$$

Therefore, the free energy per unit volume of the self-healed segment can be written as

$$W^h = \sum_{i=1}^{m} N_i^{ah}(t) n_i k_B T\left(\frac{\beta_i^h}{\tanh \beta_i^h} + \ln \frac{\beta_i^h}{\sinh \beta_i^h}\right) \tag{S27}$$

where $\beta_i^h = L^{-1}\left(\sqrt{\left[\left(\lambda^h\right)^2 + 2\left(\lambda^h\right)^{-1}\right]/3n_i}\right)$ and $N_i^{ah}(t)$ is given by **Eq. S25**. The nominal stress along λ_1 direction can be written as

$$s_1^h\left(\lambda^h, t\right) = \frac{\left(\lambda^h - \lambda^{h^{-2}}\right) k_B T}{\sqrt{3\left(\lambda^h\right)^2 + 6\left(\lambda^h\right)^{-1}}} \sum_{i=1}^{m}\left[N_i^{ah}(t)\sqrt{n_i} L^{-1}\left(\sqrt{\frac{\left(\lambda^h\right)^2 + 2\left(\lambda^h\right)^{-1}}{3n_i}}\right)\right] \tag{S28}$$

where *t* is the healing time and λ^h is the uniaxial stretch in the self-healed segment.

We consider a self-healed sample (length H) with a self-healed segment (length H^h, $H^h \ll H$) and two virgin segments (**Fig. S11**). Under a uniaxial stretch, the lengths of the whole sample and the self-healed segment become h and h^h, respectively. The stretch of the self-healed segment is $\lambda^h = h^h / H^h$. The stretch of the virgin segment is approximately equal to the stretch of the whole sample λ because $\lambda = h/H \approx \left(h - h^h\right)/\left(H - H^h\right)$. We assume the initial cross-sections of the virgin segment and the self-healed segment are the same; then, the uniaxial nominal stresses in the self-healed segment and the virgin segment should be equal, written as

$$s_1^h\left(\lambda^h\right) = s_1(\lambda) \tag{S29}$$

where $s_1^h\left(\lambda^h\right)$ is referred to **Eq. S28**, and $s_1(\lambda)$ is referred to **Eq. S7**. From **Eq. S29**, we can determine the stress-stretch behaviors of the self-healed sample for various healing time *t*.

The comparisons between the experimentally measured self-healing behaviors of the studied elastomers and theoretically calculated results are shown in **Fig. S13**. We employ an inhomogeneous chain-length distribution shown in **Fig. S13a**. The employed parameters are shown in **Table S1**. The chain dynamics parameters and Rouse friction coefficients are within the reasonable order compared with limited experimental or simulation results in the references [1, 21, 24, 25]. The theoretically calculated stress-strain curves can consistently match the experimentally measured results (**Fig. S13b**). In addition, the theoretically calculated relationships between the healing strength ratio and the healing time also agree well with the experimental results (e.g., 60°C in **Fig. S13c**).

1.3. Effect of temperature on the self-healing behavior

The temperature term is directly involved in the expression of the nominal stress of the original hydrogel and self-healed hydrogel shown in **Eqs. S7** and **S27**. However, the existence of both expressions results in the vanishing of the temperature term in the healing strength ratio. Here, we more focus on the effects of temperatures on the Rouse friction coefficient (**Eq. S13**). The curvilinear diffusivity can be affected by the temperature from two aspects: First, the temperature term explicitly appears in **Eq. S13** through k_BT. Then, the Rouse friction coefficient ξ monotonically decreases with increasing temperature [3]. This behavior can usually be modeled by Vogel relationship as [3, 21, 26],

$$\xi \propto \exp\left(\frac{B}{T - T_\infty} - A\right) \tag{S30}$$

where T_∞ is the Vogel temperature, B (positive) and A are constant parameters. By judiciously selecting these three parameters, we can quantitatively reveal the relationship between the temperature and self-healing strength ratio. Using $T_\infty = 383.2K$, $B = 486.5K$ and $A = -5.96$, we are able to theoretically capture the relationships between the healing strength ratio and the healing time, which show good agreement with experimental results for various temperatures from 40°C to 60°C (**Fig. S13c**). We further define the equilibrium healing time as the healing time corresponding to 90% healing strength ratio. We find out that the theoretically calculated relationship between the equilibrium healing time and the healing temperature is consistent with the experimental result (**Fig. S13d**).

2. Supplementary table

Table S1. Model parameters used in this paper.

Parameter	Definition	Value
k_i^{f0} (s^{-1})	Forward reaction rate	$2x10^{-7}$
k_i^{r0} (s^{-1})	Reverse reaction rate	$4x10^{-4}$
Δx (m)	The distance along the energy landscape coordinate	$1.2x10^{-9}$
b (m)	Kuhn segment length	$2x10^{-10}$
n_1	Minimum chain length	10
n_m	Maximum chain length	120
n_a	Average chain length	49
δ	Chain length distribution width	0.18
α	Chain alteration parameter	0.5
ξ (N/m)	Rouse friction coefficient	$2.4x10^{-6}$ for 60°C
T_∞ (K)	Vogel temperature	383.2
B (K)	Parameter for the Vogel relationship	486.5
A	Parameter for the Vogel relationship	-5.96

3. Supplementary figures

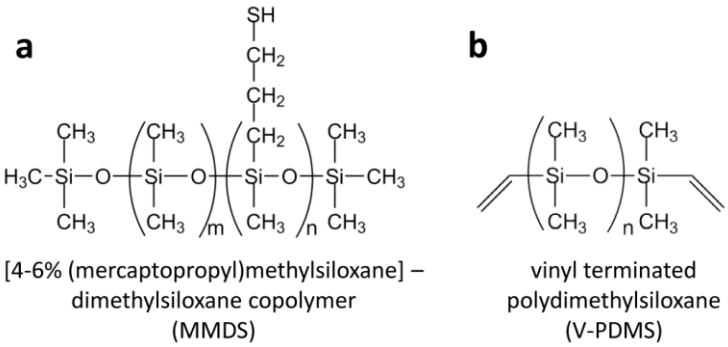

Figure S1. Chemical Structures of (a) MMDS and (b) V-PDMS.

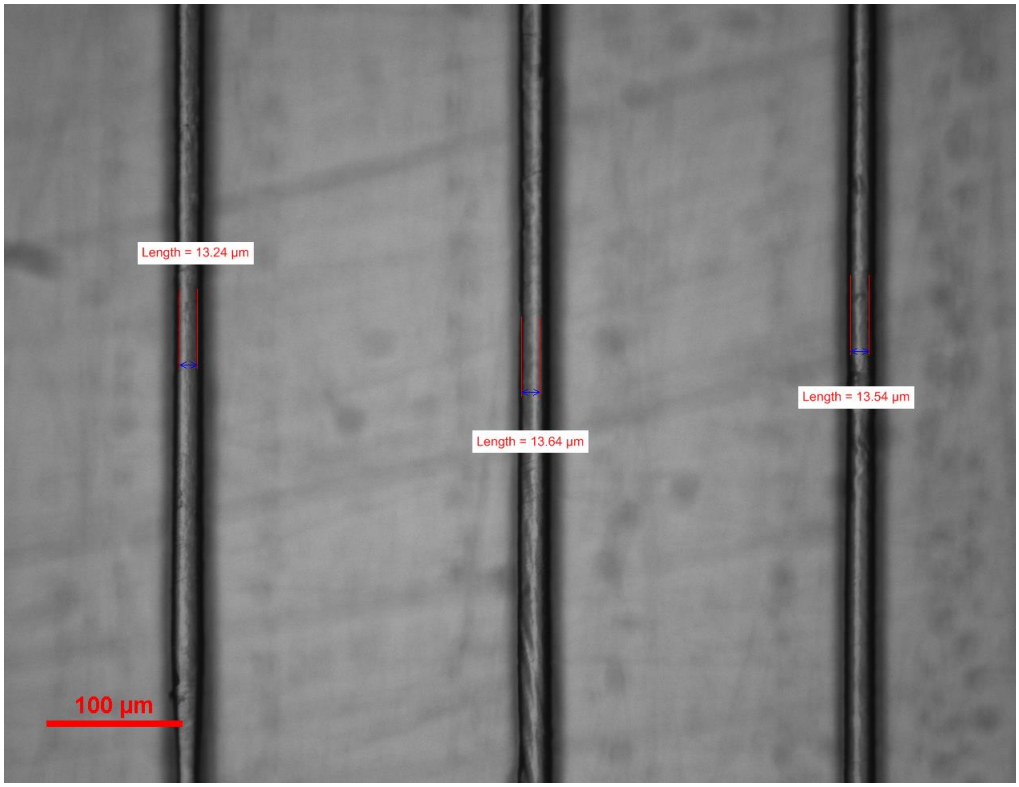

Figure S2. Microscopic image to show the manufacturing resolution. The image is taken using a Nikon microscope (Eclipse LV100ND).

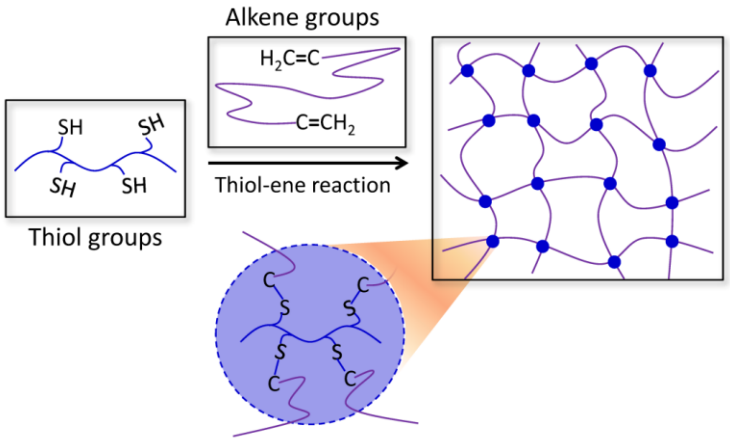

Figure S3. Molecular design of the control elastomer. MMDS and V-PDMS directly have a thiol-ene photopolymerization reaction to form an elastomer network without disulfide bonds.

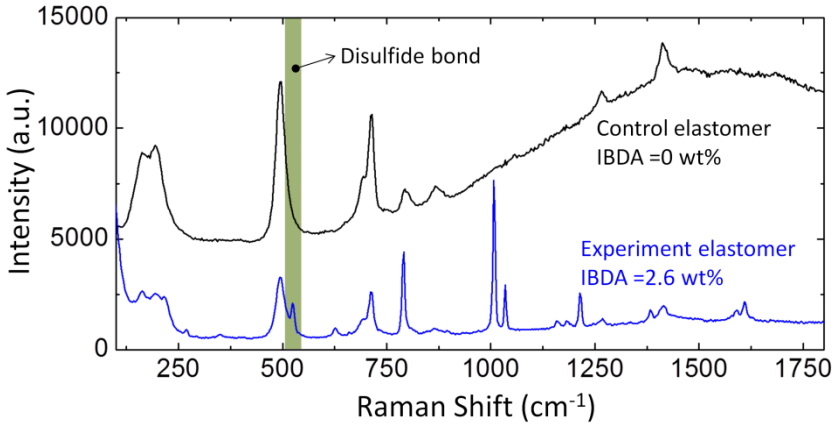

Figure S4. Raman spectra of the control elastomer (No IBDA) and the experiment elastomer (IBDA concentration 2.6wt%). The new band ~520 cm^{-1} is corresponding to the disulfide bond.

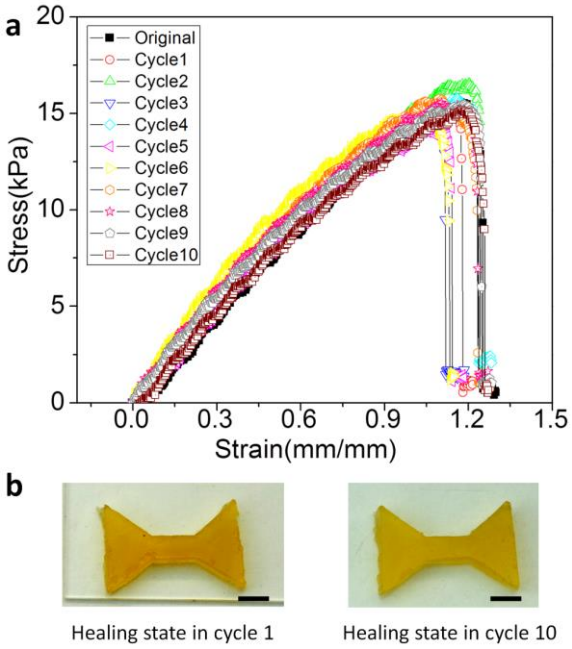

Figure S5. (a) Nominal stress-strain curves of the self-healed experiment elastomer samples after various healing cycle (each 2 h at 60°C). (b) The experiment elastomer sample at the healing state of cycles 1 ad 10. The sample does not shrink after the 10-cycle healing process. The scale bar represents 5 mm.

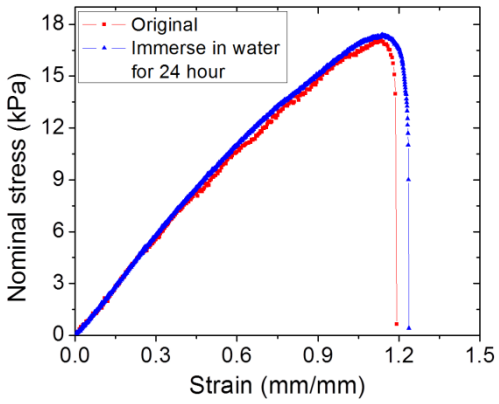

Figure S6. Nominal stress-strain curves of original experiment elastomer and the elastomer after being immersed in DI water for 24 h.

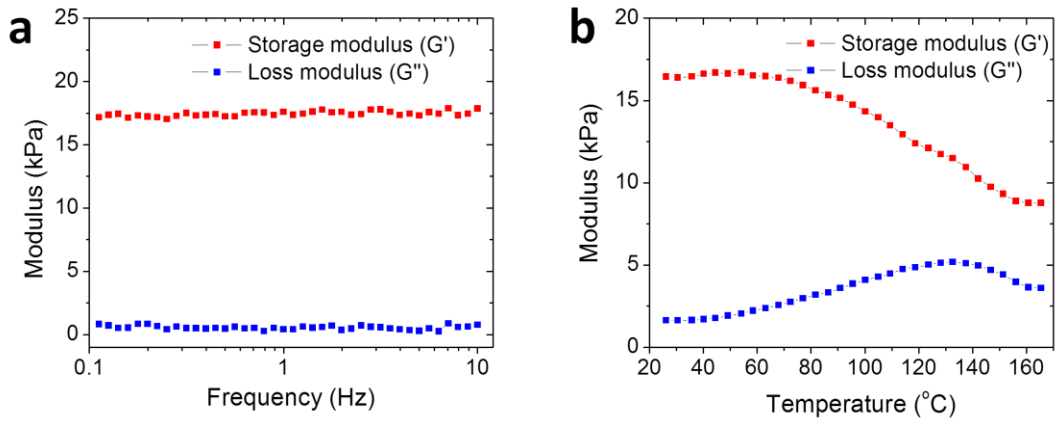

Figure S7. (a) The storage and loss moduli of the experiment elastomer over frequency 0.1-10 Hz in a frequency sweep test. (b) The storage and loss moduli of the experiment elastomer over temperature 25-165°C in a frequency sweep test with frequency 1 Hz.

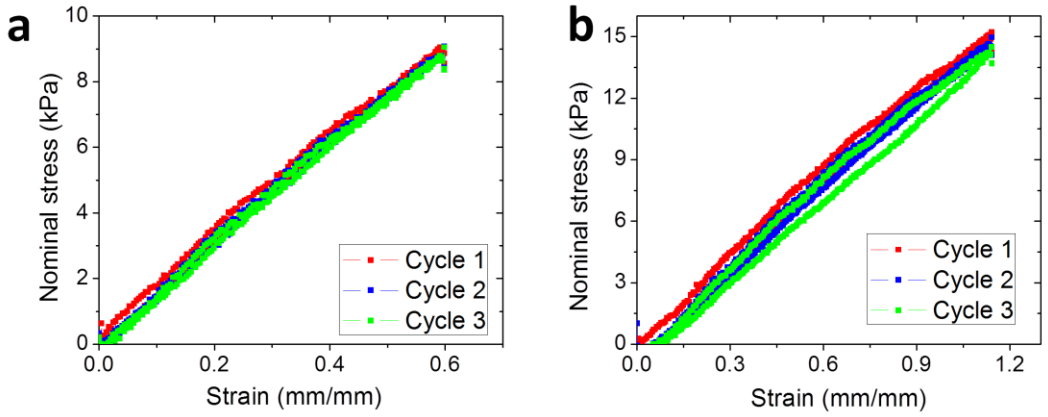

Figure S8. Nominal stress-strain curves of the experiment elastomer over three sequential tensile loading-unloading cycles with the maximal strain at (a) 0.6 mm/mm and (b) 1.1 mm/mm.

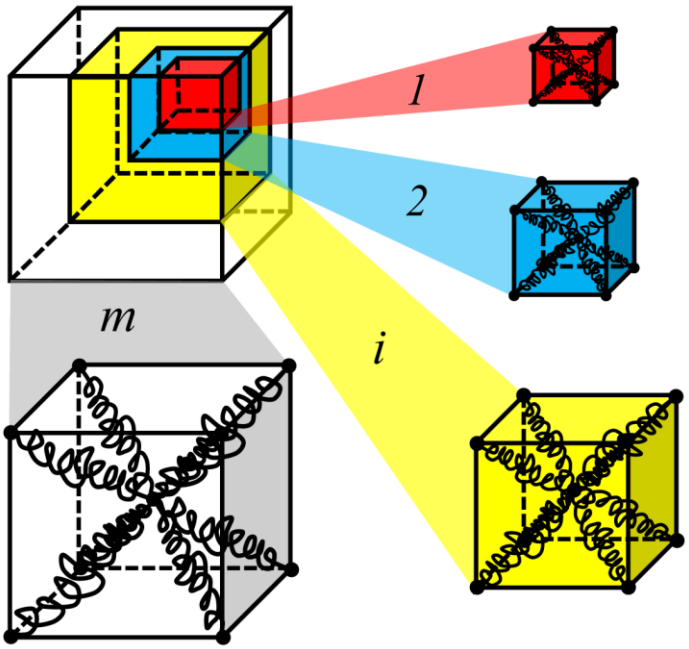

Figure S9. Schematics to illustrate an interpenetrating network model. *m* types of networks interpenetrate in the material bulk space. The *i*th network is composed of the *i*th polymer chains with Kuhn segment number n_i ($1 \le i \le m$). Each type of polymer chain self-organizes into eight-chain structures.

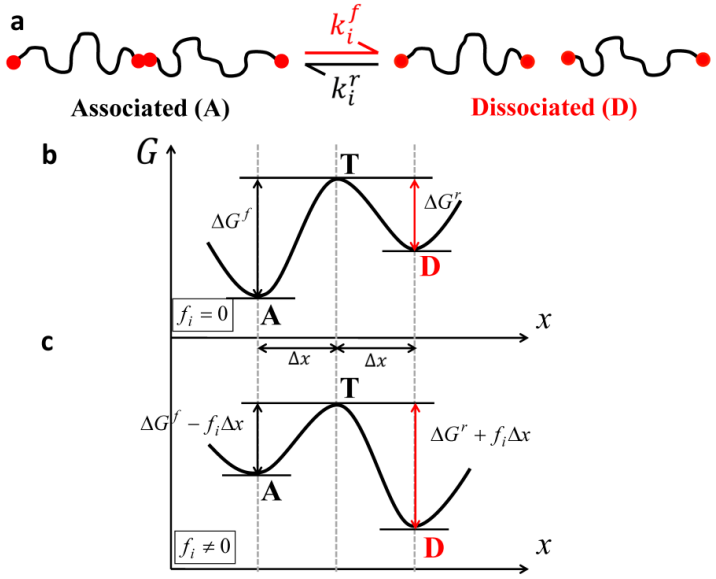

Figure S10. (a) Schematic to show the association-dissociation kinetics of the dynamic bond on the *i*th chain. We consider the reaction from the associated state to the dissociated state as the forward reaction of the *i*th chain with reaction rate k_i^f $(1 \le i \le m)$, and corresponding reaction from the dissociated state to the associated state as the reverse reaction with reaction rate k_i^r. (bc) Potential energy landscape of the reverse reaction of the dynamic bond on the *i*th chain with chain force (b) $f_i = 0$ and (c) $f_i \neq 0$. "A" stands for the associated state, "D" stands for the dissociated state, and "T" stands for the transition state.

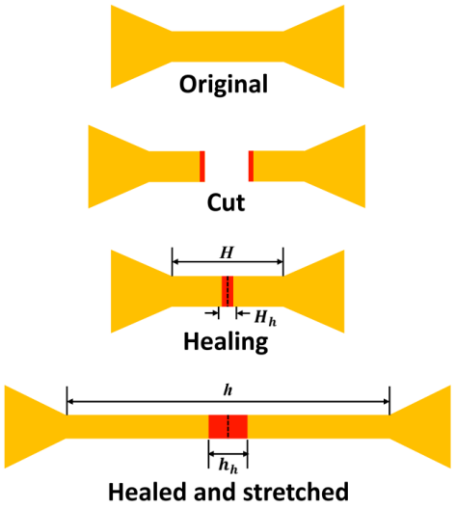

Figure S11. A schematic to show the self-healing process.

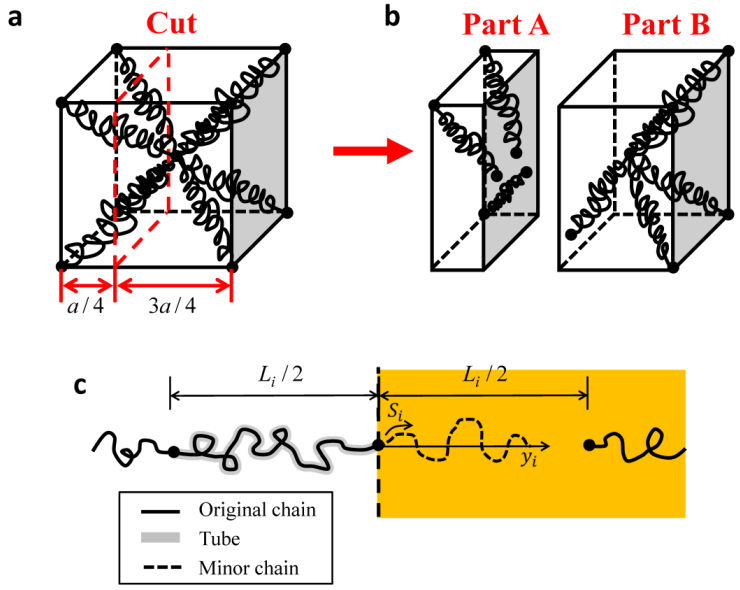

Figure S12. (a, b) Schematics of the eight-chain network model before and after the cutting process. The cutting is assumed to be located in a quarter position of the cube. (c) A schematic to show the diffusion behavior of the *i*th polymer chain across the interface.

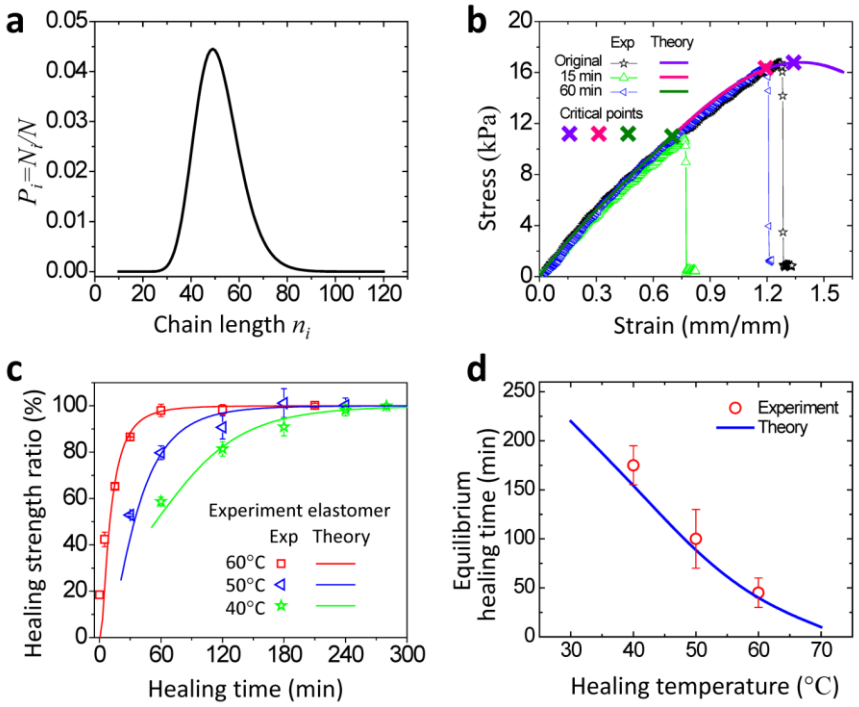

Figure S13. (a) Chain length distribution of the self-healing elastomer network. (b) The experimentally measured and theoretically calculated (b) stress-stretch curves of the original and self-healed elastomer samples, (c) healing strength ratios as a function of the healing time for various healing temperatures, and (d) the equilibrium healing time as a function of the healing temperature. The equilibrium healing time is defined as the healing time corresponding to 90% healing strength ratio.

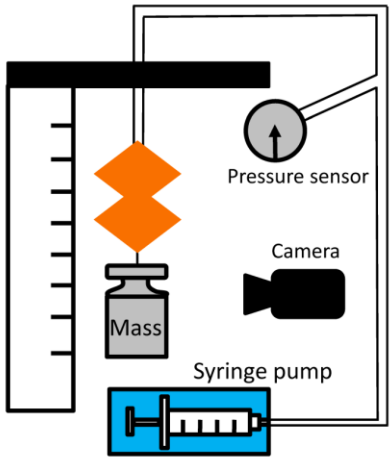

Figure S14. Experimental setup for the self-healing 3D soft actuator.

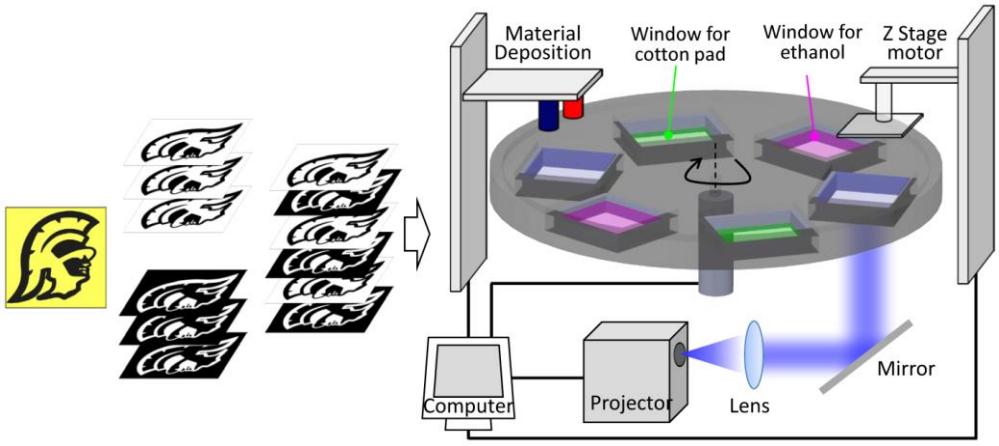

Figure S15. Schematics to show the experimental setup of the multimaterial stereolithography system.

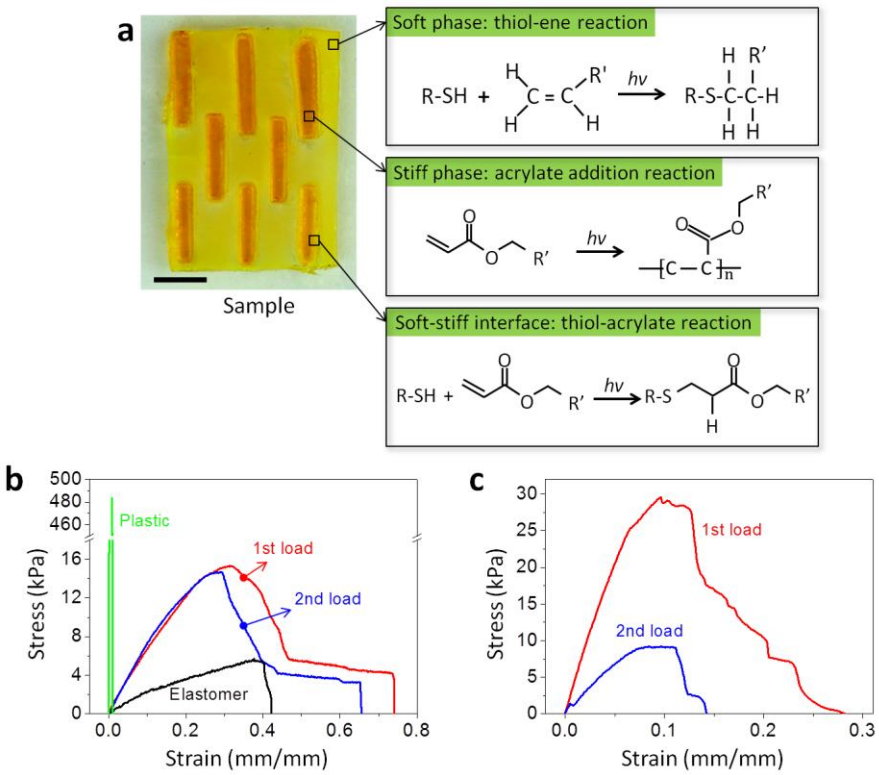

Figure S16. (a) The fabricated sample of the nacre-like stiff-soft composite. During the AM process, the soft phase undergoes a thiol-ene reaction, the stiff phase acrylate addition reaction, and the soft-stiff interface thiol-acrylate reaction. "*hv*" represents the light exposure. The scale bar represents 3 mm. (b) The uniaxial nominal stress-strain curves of the original experiment composite (1st load), the self-healed experiment composite (2nd load), pure HDDA, and pure self-healable elastomer. (c) The uniaxial nominal stress-strain curves of the original control composite (1st load) and the self-healed control composite (2nd load).

Reference

1. Wang Q, Gao Z, Yu K. Interfacial self-healing of nanocomposite hydrogels: Theory and experiment. *J. Mech. Phys. Solids.* **109**, 288-306 (2017).
2. Wang Q, Gossweiler GR, Craig SL, Zhao X. Mechanics of mechanochemically responsive elastomers. *Journal of the Mechanics and Physics of Solids* **82**, 320-344 (2015).
3. Rubinstein M, Colby R. *Polymer Physics*. Oxford University Press (2003).
4. Erman B, Mark JE. *Structures and properties of rubberlike networks*. Oxford University Press (1997).
5. Arruda EM, Boyce MC. A three-dimensional constitutive model for the large stretch behavior of rubber elastic materials. *Journal of the Mechanics and Physics of Solids* **41**, 389-412 (1993).
6. Treloar LRG. *The physics of rubber elasticity*. Oxford University Press (1975).
7. Vernerey FJ, Long R, Brighenti R. A statistically-based continuum theory for polymers with transient networks. *Journal of the Mechanics and Physics of Solids* **107**, 1-20 (2017).
8. Kramers HA. Brownian motion in a field of force and the diffusion model of chemical reactions. *Physica* **7**, 284-304 (1940).
9. Hänggi P, Talkner P, Borkovec M. Reaction-rate theory: fifty years after Kramers. *Reviews of Modern Physics* **62**, 251 (1990).
10. Stukalin EB, Cai L-H, Kumar NA, Leibler L, Rubinstein M. Self-healing of unentangled polymer networks with reversible bonds. *Macromolecules* **46**, 7525-7541 (2013).
11. Bell GI. Models for the specific adhesion of cells to cells. *Science* **200**, 618-627 (1978).
12. Ribas-Arino J, Marx D. Covalent mechanochemistry: theoretical concepts and computational tools with applications to molecular nanomechanics. *Chemical reviews* **112**, 5412-5487 (2012).
13. Marckmann G, Verron E, Gornet L, Chagnon G, Charrier P, Fort P. A theory of network alteration for the Mullins effect. *J. Mech. Phys. Solids.* **50**, 2011-2028 (2002).
14. Chagnon G, Verron E, Marckmann G, Gornet L. Development of new constitutive equations for the Mullins effect in rubber using the network alteration theory. *International Journal of Solids and Structures* **43**, 6817-6831 (2006).
15. Zhao X. A theory for large deformation and damage of interpenetrating polymer networks. *Journal of the Mechanics and Physics of Solids* **60**, 319-332 (2012).
16. Wang Q, Gao Z. A constitutive model of nanocomposite hydrogels with nanoparticle crosslinkers. *Journal of the Mechanics and Physics of Solids* **94**, 127-147 (2016).
17. de Gennes PG. Reptation of a Polymer Chain in the Presence of Fixed Obstacles. *Journal of Chemical Physics* **55**, 572-579 (1971).
18. Doi M, Edwards SF. Dynamics of concentrated polymer systems. Part 1.-Brownian motion in the equilibrium state. *J. Chem. Soc., Faraday Trans.* **74**, 1789-1801 (1978).
19. De Gennes P-G. *Scaling concepts in polymer physics*. Cornell university press (1979).
20. Kim YH, Wool RP. A theory of healing at a polymer-polymer interface. *Macromolecules* **16**, 1115-1120 (1983).
21. Whitlow SJ, Wool RP. Diffusion of polymers at interfaces: a secondary ion mass spectroscopy study. *Macromolecules* **24**, 5926-5938 (1991).
22. Zhang H, Wool RP. Concentration profile for a polymer-polymer interface. 1. Identical chemical composition and molecular weight. *Macromolecules* **22**, 3018-3021 (1989).
23. Crank J. *The mathematics of diffusion*. Oxford university press (1979).
24. Chapman BR, *et al.* Structure and dynamics of disordered tetrablock copolymers: composition and temperature dependence of local friction. *Macromolecules* **31**, 4562-4573 (1998).
25. Silberstein MN, *et al.* Modeling mechanophore activation within a viscous rubbery network. *Journal of the Mechanics and Physics of Solids* **63**, 141-153 (2014).
26. Wool RP. Self-healing materials: a review. *Soft Matter* **4**, 400-418 (2008).